TARGETED SELF-ASSEMBLY OF NANOCRYSTAL QUANTUM DOT EMITTERS USING SMART PEPTIDE LINKERS ON LIGHT EMITTING DIODES

A THESIS
SUBMITTED TO THE DEPARTMENT OF ELECTRICAL AND ELECTRONICS ENGINEERING
AND THE INSTITUTE OF ENGINEERING AND SCIENCES
OF BILKENT UNIVERSITY
IN PARTIAL FULLFILMENT OF THE REQUIREMENTS
FOR THE DEGREE OF
MASTER OF SCIENCE

By
Gülis Zengin
August 2008

I certify that I have read this thesis and that in my opinion it is fully adequate, in scope and in quality, as a thesis for the degree of Master of Science.

Assist. Prof. Dr. Hilmi Volkan Demir (Supervisor)

I certify that I have read this thesis and that in my opinion it is fully adequate, in scope and in quality, as a thesis for the degree of Master of Science.

Prof. Dr. Ergin Atalar

I certify that I have read this thesis and that in my opinion it is fully adequate, in scope and in quality, as a thesis for the degree of Master of Science.

Assoc. Prof. Dr. Rengül Çetin-Atalay

Approved for the Institute of Engineering and Sciences:

Prof. Dr. Mehmet B. Baray
Director of Institute of Engineering and Sciences

ABSTRACT

TARGETED SELF ASSEMBLY OF NANOCRYSTAL QUANTUM DOT EMITTERS USING SMART PEPTIDE LINKERS ON LIGHT EMITTING DIODES

Gülis Zengin
M.S. in Electrical and Electronics Engineering

Supervisor: Assist. Prof. Dr. Hilmi Volkan Demir
August 2008

Semiconductor nanocrystal quantum dots find several applications in nanotechnology. Particularly in device applications, such quantum dots are typically required to be assembled with specific distribution in space for enhanced functionality and placed at desired spatial locations on the device which commonly has several diverse material components. In conventional approaches, self-assembly of nanocrystals typically takes place nonspecifically without surface recognition of materials and cannot meet these requirements. To remedy these issues, we proposed and demonstrated uniform, controlled, and targeted self-assembly of quantum dot emitters on multi-material devices by using cross-specificity of genetically engineered peptides as smart linkers and achieved directed immobilization of these quantum dot emitters decorated with peptides only on the targeted specific regions of our color-conversion LEDs. Our peptide decorated quantum dots exhibited 270 times stronger photoluminescence intensity compared to their negative control groups.

Keywords: self-assembly, nanocrystals, quantum dots, light emitting diodes, inorganic binding peptides, cross-specificity, optoelectronics, nanophotonics.

ÖZET

AKILLI PEPTİD BAĞLAYICILARI KULLANARAK NANOKRİSTAL KUVANTUM NOKTACIK IŞIYICILARININ IŞIK YAYAN DİYOTLAR ÜZERİNDE YÜZEY MALZEMESİNE ÖZGÜ OLARAK KENDİ KENDİNE DÜZENLENMESİ

Gülis Zengin
Elektrik ve Elektronik Mühendisliği Bölümü Yüksek Lisans
Tez Yöneticisi: Yard. Doç. Dr. Hilmi Volkan Demir
Ağustos 2008

Yarıiletken nanokristal kuvantum noktacıklarının nanoteknolojide birçok kullanım alanı bulunmaktadır. Özellikle aygıt uygulamalarında, aygıtların daha etkili bir şekilde çalışabilmesi için nanokristallerin yüzeyin belirli bölgelerinde kendi kendine düzenlenerek birçok farklı malzemelerden yapılmış olan bu aygıtların sadece istenilen bölgelerine tutunması gerekmektedir. Nanokristallerin yüzeye tutunmasında kullanılan klasik yöntemlerde, nanokristaller genelde yüzeyi tanımadan malzemeye özgü bağlanma olmaksızın tutunmaktadır. Bu yüzden klasik yaklaşımlarla yüzeye tutundurulan nanokristaller, aygıt tasarımlarında istenilen özgü bağlanmayı sağlamamaktadır. Bu ilgili problemleri çözmek üzere, birden fazla malzemeden yapılmış olan aygıtlar üzerinde, nanokristallerin homojen, kontrollü ve yüzey malzemesine özgü olarak kendi kendine düzenlenmesini önerdik ve gösterdik. Bunu, malzemeye özgü olarak bağlanabilen genetik olarak tasarlanmış peptitleri akıllı bağlayıcı olarak kullanarak başardık. Bu peptitlerle kuvantum noktacık ışıyıcılarının etrafını kaplayarak oluşan melez nanoyapıların ışık yayan diyotlar (LEDler) üzerinde sadece istenilen bölgelere tutunmasını sağladık. Bu şekilde oluşturulan örneklerde, akıllı peptitlerle kaplanmamış örneklere göre 270 kat daha fazla fotoışıma elde ettik.

Acknowledgements

I would like to thank Prof. Hilmi Volkan Demir for inspiring me and helping me start my studies at Bilkent University as my supervisor. For these two years, he has been a great mentor for me with his wisdom, extensive experience and great depth of knowledge. I would also like to thank him especially for his unfaltering enthusiasm, incredible kindness, and support when I am navigating through a few rough seas.

I would like to thank to the faculty members at Bilkent University who have shared their knowledge and wisdom with me. I specially thank to Prof. Ergin Atalar and Prof. Rengul Cetin-Atalay for being thesis committee members and for their efforts in finalizing this thesis.

I would like to thank Prof. Mehmet Sarikaya and Prof. Candan Tamerler for their creative and constructive collaborations. I would especially like to thank Urartu Ozgur Safak Seker whose help and strong support made this thesis possible.

While working in a group like Demir Group, it is simply impossible to thank each and everyone for their support and friendship. Here simply, I would like to thank everyone who took the time to discuss things with me and helped me. It was a pleasure for me to work with them as a team.

I would also like to thank all staff and researchers of Department of Electrical Electronics Engineering, Nanotechnology Research Center, Advanced Research Laboratory, and Institute of Material Science and Nanotechnology. Without their help and support behind the scenes, it would not be possible to go so far on this work.

Last but not least, I would like to thank my friends and my family.

Table of Contents

List of Figures

List of Tables

Chapter 1

Introduction

Semiconductor quantum dot nanocrystals have widely being exploited in many photonic devices such as light emitting diodes, solar cells, lasers, photodetectors and modulators for their unique electronic and optical properties [1-4]. Assembling of quantum dots in two or three dimensions on the nanometer scale in these devices has been extremely important for device performance [5]. In most optoelectronic device applications, the structure contains three main materials: semiconductor, metal, and dielectric materials. High density of quantum dots are desired to be uniformly located on a specific part of the device, for instance on optical window of a light emitting diode for device efficiency [4]. Quantum dot nanocrystals have conventionally been immobilized on a surface using coulombic interactions, hydrogen bonding or van der Waals forces [6-9]. In optoelectronic device applications, typically chemical linkers, or oppositely charged linkers and surfaces have been used for integration purposes [10]. Quantum dots are also packed in a host polymer for immobilization on the device surface. For instance, in a recent study of our group for white light generation using CdSe/ZnS core shell quantum dots hybridized with light emitting diodes, quantum dots were prepared in poly(methyl methacrylate) (PMMA) and then the host polymer was evaporated to complete polymerization process in each layer of quantum dot films [11]. Therefore, in none of these device applications quantum dots were assembled on the device surface by recognizing the surface material or the part where they must be specifically located on the device. Such non-specific assembly has been disadvantageous for device performance and as well as excess use of quantum dots in non-required parts. Immobilization of quantum dots only on the optical window in a white light emitting diode is absolutely necessary owing to the fact that quantum dots are pumped through emission from such optical windows of LEDs and quantum dots assembled on the metal parts or the semiconductor parts out of the emission cone are not pumped and thus they do not contribute to overall luminescence of the hybrid device. On top of being an advantage to avoid excess use of quantum dots on non-contributive parts, quantum dot layers on metal contacts obstruct the electrical connection between contacts and wire or probe to electrical supply, which further makes it difficult to drive the LED. This became motivation for us to investigate material specific self-assembly of quantum dots on targeted surfaces of LEDs. In other words, we develop a strategy to enable quantum dots to recognize the parts that they have to bind on the device surface and then uniformly self assemble on these parts of the device by showing strong affinity towards these particular regions on the surface. To address this need, we propose and demonstrate hybridizing quantum dots with genetically engineered peptides, which are designed to recognize and then bind to the desired material. In this thesis, we show targeted self-assembly of peptide hybridized quantum dots on specific LED surfaces. We also study building layer-by-layer quantum dot assemblies on top of each other by the assistance of peptides. In addition to use of peptides to assemble quantum dots on LED surface by means of showing specific affinity to targeted material, we also exploit peptides to form a separating layer between two peptide hybridized quantum dot layers by regulating biomineralization of intermediate silica layers. Therefore, here we utilize bifunctionality of smart peptides to design more efficient and novel inorganic-organic hybrid devices.

In the direction of this motivation presented here, this thesis is organized as follows. In the first chapter we give a brief introduction to the subject and our motivations of this thesis research work. Our solution to the non-specific self-assembly problem and our contribution are presented in this chapter. In the second chapter, an overview of nanocrystal quantum dot emitters are explained with examples from optoelectronic device applications, and bio- and nanotechnology. In the third chapter, the different known techniques for immobilization of quantum dots and their wide range of applications are discussed, presenting their pros and cons. In the fourth chapter, importance of smart peptides and their use in the assembly of nanostructures are introduced, along with the techniques used for formation of these peptides. In the fifth chapter, our nanocrystal hybridized LEDs for the purpose of white light generation are described. Also, tuning color parameters of white light by changing nanocrystal thickness, concentration, and order is presented. In the sixth chapter, we demonstrate how to self assemble quantum dots with peptide assistance on multi-material patterned surfaces and devices with two methods, first with the conventional method and second with our proposed innovative approach. Then we discuss the results of these two approaches with several characterization measurements. Subsequently, we examine the cross specific binding of peptide hybridized quantum dots on dielectric, metal, and semiconductor patterned real optoelectronic chips with our innovative approach. We then introduce the immobilization of peptide hybridized quantum dots on LED surface in the future to be used in color conversion lighting applications. Moreover, we show another important feature of peptides in addition to targeted self-assembly of quantum dots on a desired surface, which is the use of peptides as regulators in silica biomineralization for layer-by-layer design of quantum dots in optoelectronic device applications. In the last chapter, we present the highlights of our thesis research work and the future prospects of our new device designs.

Chapter 2

Semiconductor quantum dot nanocrystals

2.1 Overview

Semiconductor colloidal quantum dots have been extensively used in many fundamental or applied studies such as LEDs, diode lasers, transistors, photovoltaics, biolabeling, and medical imaging [1-4, 12-16]. Their typical core sizes vary between 15 and 120 Å in diameter [17-19]. In semiconductor quantum dots electrons and holes are confined in three dimensions more than Bohr radius, which is the typical distance between an electron and hole in bulk semiconductors. This spatial confinement gives rise to discrete electron and hole energies in a quantum dot and it is the origin of their electrical and size dependent optical properties such as optical absorption, photoluminescence (PL), and electroluminescence (EL) at discrete energy levels [20-24]. They also show characteristics in between bulk and discrete molecules. Similar to a bulk semiconductor, wave functions of quantum dots penetrate into the crystal lattice, which has a characteristic of a periodic potential owing to the atomic arrangement. However, a quantum dot is comparable to a molecule since it possesses density of states and an energy spectrum which are quantized near the band gap energy [25].

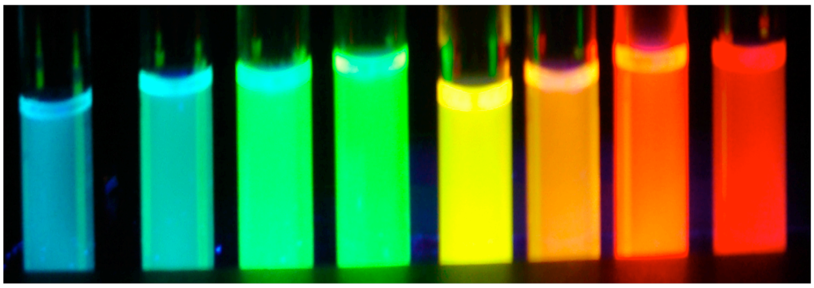

Figure 2.1 - Fluorescence of CdSe nanocrystal quantum dots with different size under excitation in ultraviolet.

One of the most important optical features of semiconductor colloidal quantum dots is the emission spectrum in a wide range of wavelength. The materials used determine their intrinsic energy levels; therefore, emission spectra. For example, while ZnSe, CdS, CdSe, and CdTe nanocrystals have visible emission spectra whereas InAs, InP, and PbS nanocrystals have emission spectra broadening into the near-IR. CdSe nanocrystals show wide-range of absorption spectra [17, 26, 27]. On the other hand, quantum dots with different sizes have different emission spectra even though they are made of identical materials (Figure 2.2A), since at the energy levels close to band gap energy of the material, confinement size becomes dominant in determining the emission wavelength. For instance, emission spectrum shifts to longer wavelengths (lower energy) with increasing particle size (Figure 2.2B). Emission spectra of semiconductor colloidal quantum dots directly depend on band gap energy and discrete energy levels. Smaller quantum dots possess bigger discrete energy levels; therefore, they are able to absorb photons with higher energy. Absorption characteristics of quantum dots make it possible to excite many different sized quantum dots at the same time with a single excitation wavelength and obtain a wide range of visible emission spectrum from a single wavelength emission of each quantum dots. In quantum dots, the core semiconductor part such as CdSe can be coated with a wider band gap semiconductor such as ZnS or CdS as a shell. This method mainly depends on the concepts of band-gap engineering used in electronics With this method, the surface trap states are passivated and flow of excitons to the outside of the core is minimized, so it improves stability and quantum efficiency of quantum dot without considerably having an effect on the emission spectrum [28-30].

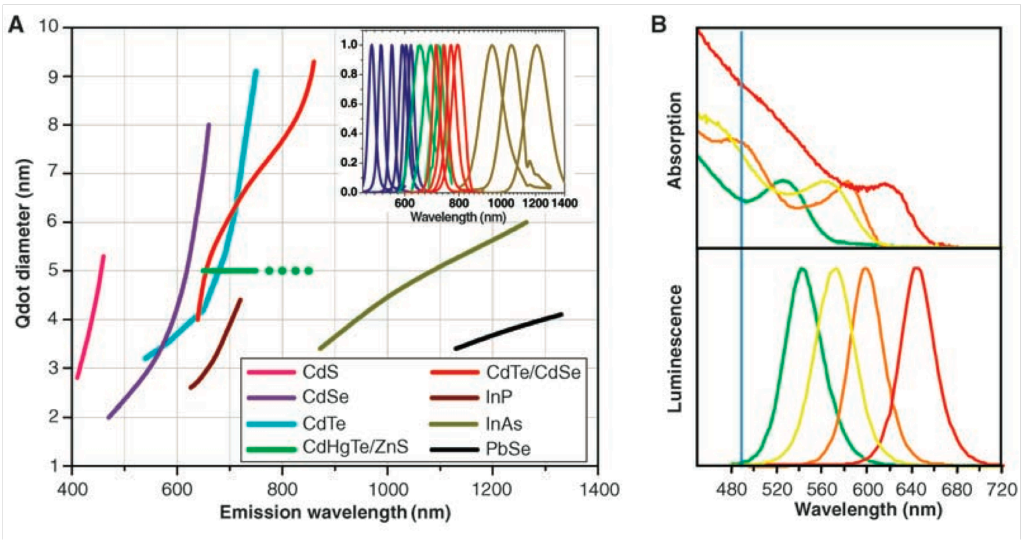

Figure 2.2 – (A) Emission spectra of quantum dots with respect to sizes of quantum dots which were synthesized from different semiconductor materials. (B) Absorption (upper panel) and emission (lower panel) spectra of CdSe/ZnS quantum dots. Green, yellow, orange and red emitting quantum dots are given. All of them were excited with 488 nm laser at the same time (shown with blue vertical line) [31].

2.2 Synthesis of semiconductor quantum dot nanocrystals

Nanocrystals can be synthesized through hot injection method, a synthesis process for monodisperse colloidal semiconductor quantum dots with high quantum efficiency [17, 32, 33]. In our research group, CdSe/ZnS quantum dot nanocrystals are synthesized with the same method using 1 gr HdA, 1 gr TOPO, 6 ml octadecene, 0.1 M 2 ml for the synthesis of Cd solution for CdSe core quantum dots. For the synthesis, the mixture of these materials is heated in a nanocrystal synthesis flask. A nanocrystal synthesis flask is composed of a condenser, a tube for argon gas entrance, a heater, a stirrer, a temperature controller, and a tube for adding each substance. After temperature reaches to a certain value, Se solution is put in the flask through one of the entrance tubes inside the glove box to avoid contact with oxygen. The chemical reaction begins with the injection of 2 ml 0.1 M Se solution into the flask. The most important properties of quantum dots, i.e., size and emission wavelength, are controlled by reaction time and temperature. For instance, increasing the reaction time shifts the wavelength from green to red. For cooling, the hot flask is placed into water to cool it down after reaction ends. Hexane is added into the solution in a new flask then the mixture remains for couple of hours for phase separation, and finally the total solution is placed in another flask [34].

2.3 Application examples

2.3.1 Biology

In biological sciences, many type of fluorophores such as organic dyes have been used for imaging, labelling and sensing. However, traditional dyes have significant drawbacks such as narrow excitation, and broad absorption spectra, low photostability which means low photobleaching thresholds, and short fluorescent life time when compared to quantum dot nanocrystals [35, 36]. Therefore, quantum dot nanocrystals have been very interesting since they address these limitations of conventional dyes with their unique optical properties both in vitro and in vivo biological studies. Unlike traditional dyes they have wide range of absorption spectra, many quantum dots with different emission wavelength can be concurrently excited by a single excitation wavelength [31, 35]. Quantum dots also have narrower emission spectra, which enables them to be used in simultaneous detection of multiple signals, which is called multiplexing [36]. Moreover, they are stable and can be excited multiple times without easily bleaching and they exhibit high luminescence intensity at the same time. Further, they have a longer fluorescent lifetime, which is slower than background decay; therefore, they have smaller signal-to-noise ratio which is advantageous in imaging [37].

Main applications of semiconductor colloidal quantum dot nanocrystals in biological sciences include fluorescence resonance energy transfer (FRET), gene technology, labelling, cell tracking, pathogen and toxin detection, in vivo animal imaging and tumor biology investigation [35]. Labelling of cells is one the major biological applications of quantum dots which has attracted the greatest attention. With quantum dot labelling of cells it is possible to obtain high resolution three dimensional multicolor images as well as real-time imaging over long periods of times under continuous illumination. Real-time imaging of single-cell migration likely has significant influences in many research areas such as cancer metastasis, and immunology. So far, it is reported that this technology has been used in labelling of DNA arrays, fixed cells and tissues, membrane proteins, microtubules, nuclear antigens, and chromosomes [31]. Moreover, there is on going research on use of quantum dots in vivo whole-animal imaging to issue the problem of possible toxicity of quantum dots both in animal and human applications [31, 35-36].

2.3.2 Photovoltaics

Photovoltaics, made of semiconductors especially silicon, is used to convert light energy into electrical energy. While this conversion is achieved by silicon efficiently, manufacturing costs of silicon cells still remains quite high and other type of cheaper semiconductor cannot provide the same conversion efficiency as silicon. As a solution to this cost and efficiency problem, a thin film of quantum dot nanocrystals deposited on photovoltaic surface by spin coating can be a solution with unique abilities of quantum dots to interact with light. By engineering the size and type of the quantum dot nanocrystals, the solar cells can be tuned to absorb different wavelengths of the solar light spectrum [12, 38, 39]. In a solar cell, while one photon of light can release one electron from silicon, photons with high energy such as blue or ultraviolet can free two or more electrons from semiconductor quantum dot nanocrystals. It was showed that quantum dot nanocrystals made of lead selenide could generate up to seven electrons per photon when they ere exposed to high-energy ultraviolet light [38]. Further, since synthesis of quantum dot nanocrystal can be achieved using simple chemical reactions, they could also make solar cells far less expensive. It was reported that quantum dot based photovoltaics could have maximum conversion efficiency of 42 percent, which is significantly better than the maximum efficiency of silicon, 31 percent. On the other hand, quantum dot based solar cells have not been commercialized yet, but they are still promising for cheap and abundant solar power source [12].

Chapter 3

Self-assembly techniques of nanoparticles

3.1 Overview

It is well known that for developing next generation nanostructure based device applications, the ability to build well defined and defect-free ordered two- and three-dimensional structures on the nanometer scale are very important [5]. For that reason, ordering of nanostructures through different, creative and pioneering methods has recently gained more importance. Nanostructure can be ordered and assembled mainly with two methods: top-down or bottom-up. Top-down methods include printing, patterning and lithography while bottom-up methods are based on self-assembly techniques [40]. Self-assembly is based on specific noncovalent interactions and is commonly utilized by organisms for the formation of hierarchical and complicated biological structures. Biological molecules, polymers, inorganic materials and many other structures have been assembled by mimicking the way nature uses self-assembly technique for organization of nanostructures [41, 42]. In the subsequent sections, different approaches for nanostructure assembly are briefly described with major principals of each method.

3.2 Evaporation-induced self-assembly

This method is based on slow drying or evaporation of the solvent to construct well-ordered, self-assembled nanostructures on the surface. During the evaporation of the solvent, comparatively frail forces attraction forces between nanostructures in the solvent make these nanostructures to order themselves. This process is affected by temperature, concentration and dynamics of the drying solvent. It is possible to obtain different forms of nanostructures by selecting different solvents, size of nanoparticles and thermodynamic states [43-45]. As seen from Figure 3.1, during the drying of the solvent on a hydrophilic surface, nanoparticles are forced to drift towards evaporating ends and then in the most recent evaporating ends, there will be less accumulation of nanoparticles and these ends become thinner than other ends of the substrate [40]. If nanoparticles diffuse quickly than the solvent evaporates, the nanoparticles will accumulate more underneath of the surface. It will probably lead formation of a 2D monolayer at the surface by self-assembly due to the tension between nanoparticles and the surface. Generally this self-assembly of nanoparticles is feasible when the nanoparticles are forced to diffuse towards the solvent surface [46]. While this method is an important approach to build multifunction structures and devices, it is also simple, cheap and powerful for self-assembling of many kinds of nanoparticles. This strategy depends on the principles of the electrostatic forces, surface tension and morphology and size and shape of the nanoparticles [47].

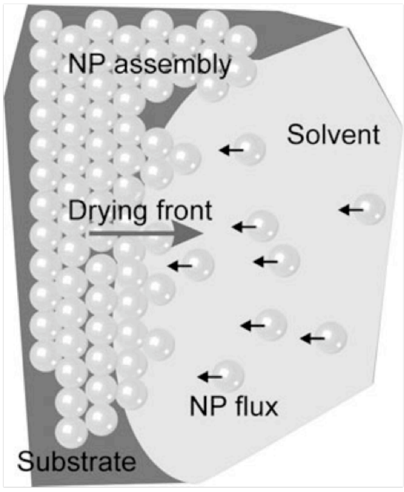

Figure 3.1 – Drying-assisted assembly of nanoparticles on a hydrophilic substrate surface [40].

3.3 Chemical self-assembly

Similar to drying-assisted assembly technique, this method is also a robust tool to build well-ordered self-assemblies of nanoparticles both in solution and in film. This strategy is primarily based on covalent bonding of functionalized groups covering the surface of nanoparticles and substrate surface in addition to non-covalent bonds which results the ordering of nanoparticles. Electrostatic layer-by-layer assembly, hydrogen bonds mediated assembly, chemically template assisted assembly and self-assembled monolayers (SAMs) are some of the specific examples based on this technique [48, 49].

In self-assembled monolayers, organic molecules, which have appropriate chemical end groups on their surfaces, are organized onto appropriately functionalized substrate surfaces. There are two different approaches for building SAMs on surfaces. In the first method, surface of the substrate (typically glass or silicon substrates) is coated with silane or similar molecules such siloxanes, Figure 3.2 A. This process is called silanation or silanization of substrate surface. The second method involves sulphur coinage-metal covalent bonds on Au or Ag surfaces as illustrated in Figure 3.2 B [40, 49, 50].

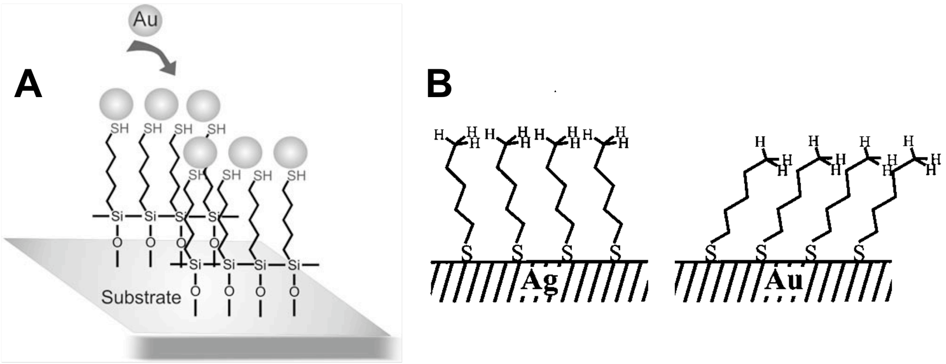

Figure 3.2 – Self-assembled monolayers are given. (A) Ordering of Au nanoparticles on self-assembled monolayers of thiols on a silicon substrate which was formed by silanation [40]. (B) Self assembled monolayers of alkanethiol on Ag and Au surfaces [49].

Another type of chemically assisted assembly is based on hydrogen bonding. For instance, barbituric acid stabilized Au nanoparticles can been assembled on Hamilton-type receptors coated Au surface by formation of several hydrogen bonds between barbituric acid molecules and Hamilton-type receptors [51].

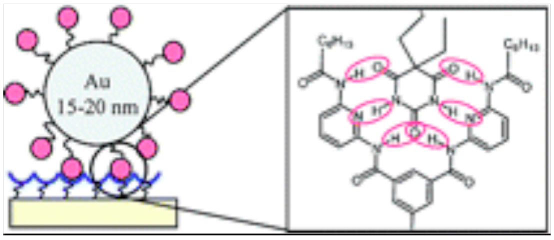

Figure 3.3 –Assembly of Au nanoparticles on Au substrate by using hydrogen bonding [51].

Furthermore, use of some biomolecular linkers for assembly of nanoparticles depends on hydrogen bonding such as interactions between two complementary DNA strands, antigen and antibody or biotin and streptavidin [40].

Electrostatic forces can also be used for building highly ordered layer-by-layer structures. Polyelectrolytes, DNA, proteins and many other nanoparticles can be assembled with layer-by-layer technique in many practical applications such as light emitting diodes, single electron devices and biosensors [40, 52].

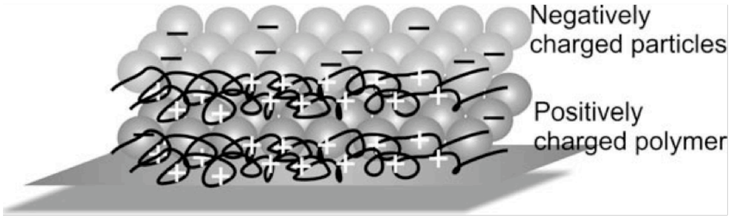

Figure 3.4 – Layer-by-layer assembly technique for immobilization of negatively charged nanoparticles on positively charged polymer via electrostatic interaction between nanoparticles and polymer [40].

This approach is advantageous for having precise control of interactions among nanoparticle layers or interactions between substrate and nanoparticles by controlling thickness of nanoparticle and separating intermediate layers. It is possible to assemble up to 1000 layers of nanoparticle films with commercially available instruments [53].

3.4 Electric or magnetic field assisted self-assembly

Nanoparticles can also be self-assembled and ordered in directional manner even in 3D by applying electric and magnetic fields. Changing the direction of the applied field also alters the orientation of growth. An example of electric-field assisted assembly is the formation of Au microwires by ordering metal nanoparticles dispersed in a solution by applying electric field. Alternating electric field (dielectrophoresis, DEP) changes the mobility and interactions of nanoparticles and each nanoparticle assembles to build the wire in the direction of the field gradient [54].

3.5 Template-assisted assembly

Self-assembly of nanoparticles on surfaces can be eased by utilization of templates as a host. Templates can be made of inorganic or biological materials. Alumina nanoholes, inorganic nanowires or carbon nanotubes are some examples of inorganic templates and they are practical to supply toughness for the assembly of nanoparticles [40, 55].

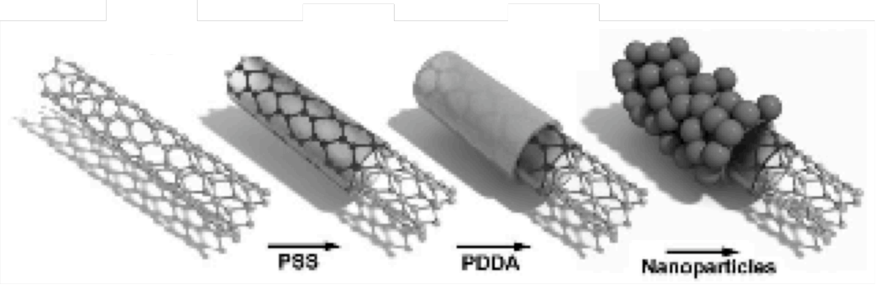

Figure 3.5 -Carbon nanotube as an inorganic template for self-assembly of nanoparticles [55].

Biological molecules such as DNA strands, peptides and viruses have been extensively studied in order to provide a template for self-assembly of nanoparticles though covalent or non-covalent bonding [5, 56-62]. With this approach, it is possible to direct the assembly of streptavidin-conjugated CdSe/ZnS core/shell quantum dots into well-defined periodic patterns with use of biotin added two-dimensional DNA-tile arrays as illustrated in Figure 3.6 [56].

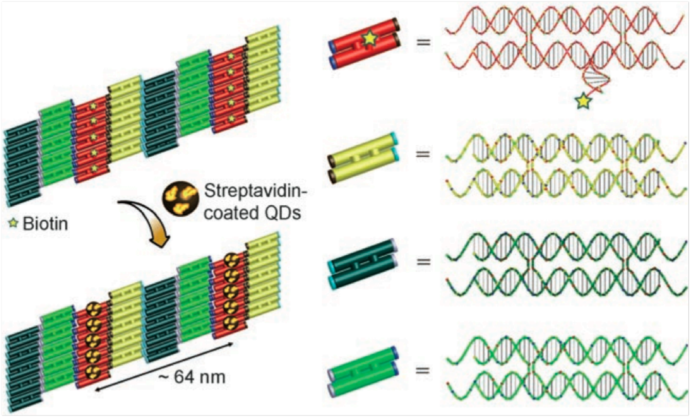

Figure 3.6- DNA assisted self-assembly of Quantum Dots into 2D [56].

Using genetically engineered viruses as template is an alternative way of self-assembly of nanoparticles. In this technique, viruses are selected by combinatorial phage display method such that their coating proteins on the virus surface will specifically recognize surface material and bind to nanoparticles. These specific recognition properties of the virus can be used to organize inorganic quantum dots to form ordered arrays. With this approach, it is possible to change both the length of virus and the type of inorganic materials through genetic modification and selection [5]. An example of viral assembly of ZnS quantum dot nanocrystals to build ZnS nanowires by using genetically engineering coating proteins of M13 bacteriophage virus can be seen in Figure 3.7 [63].

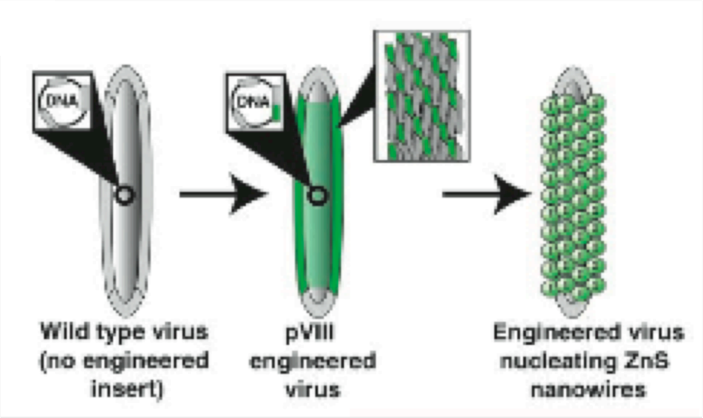

Figure 3.7 – Self assembly of ZnS quantum dot nanocrystals using genetically engineered M13 bacteriophage virus to create ZnS nanowires [63].

Another example of self-assembly of nanoparticles was reported by using cage like proteins, which show specific binding to some selected inorganic materials such as Ti. Sano et. al. showed the self-assembly of Fe, Co and CdSe nanoparticles by placing these nanoparticles inside cage proteins which are able to recognize Ti surface. [58, 59].

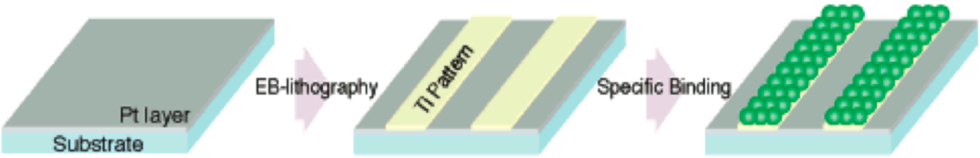

Figure 3.8 – Cage protein assisted self-assembly of nanoparticles on Ti surface [59].

Chapter 4

Genetically Engineered Peptides for Inorganics

4.1 Biomimetics

Biomimetics is a technique to design novel structures and systems by exploiting methods used by living organisms in nature. Adapting mechanisms of nature to build synthetic structures is attractive since evolutionary changes compel the living organisms to optimize biological methods to construct structures such that they are effective and efficient at the same time. For that reason by inspiring from nature, molecular biomimetics has become a promising research area to make practical material and devices in nanotechnology and in other fields [62, 64, 65].

A typical example of biomimetics is lotus flower plant. Lotus plant is famous for its superhydrophobic leaves, which are exceptionally unsticky for any kind of liquids. When water drops fall on lotus leaves, water drops accumulate all dust and dirt on the lotus surface. This lotus effect has inspired many researchers to design superhydrophobic and self-cleaning surfaces such as paints, glasses and fabrics [66].

Another important application of biomimetics is genetically engineered peptides for inorganics (GEPIs). For millions of years living organisms have been using proteins as a tool to carry out many activities through their specific recognition and interactions in biological systems. Inspiring from living organisms, polypeptides can be genetically engineered as molecular smart linkers to specifically bind to selected inorganic materials for building novel and innovative structure and device applications in nanotechnology [60, 67].

4.2 Genetically engineered peptides for inorganics (GEPI)

Using genetically engineered peptides as smart molecular linkers for self-assembly of inorganic nanoparticles to build more complex structures in many device architecture is desirable because specifically self-assembling nanoparticles at targeted locations on device surface is indispensible for device performance and efficiency. Fundamentals of genetically engineered peptides are based on mimicking how living organisms use peptides and proteins to control formation of many biological structures. Since many years of evolutionary processes lead to specific molecular recognition mechanism of peptides and proteins in biological systems, genetically engineered peptides for inorganics uses the same principle [65, 67]. As living organisms utilize peptides for building structures in mild conditions, self-assembly of nanoparticles by using genetically engineered peptides similarly takes place in softer conditions while conventional deposition and assembly techniques generally require tougher conditions such as high temperature, low pressure, highly acidic or basic environment or involvement of many chemicals. The most important and distinguishing feature of inorganic binding peptides from other type of linkers is ability to recognize targeted inorganic material and to bind this material surface by showing strong affinity towards it. To design these specific inorganic binding peptides, current knowledge and techniques of protein design are not adequate; therefore, from very large arbitrarily produced libraries, peptides can be screened and selected for their binding activity to desired inorganic surfaces using phage and cell-surface display techniques [60].

In these techniques arbitrary sequences of amino acids, encoded within a phage genome or on a plasmid, so that they are displayed on the surface of the virus or bacterial cell as coating proteins on phages and membrane proteins bacterial cells on respectively (Figure 4.1). It is possible to select these peptides for metals, oxides, minerals and semiconductors by using these techniques. Our collaborators group has so far identified more than 1000 peptides binding to a variety of inorganics (Figure 4.2) [64]. Subsequently a chemical-based elution protocol is carried out for the selection of the strong binding peptides followed by several washing and elution cycles. Once the strong binding peptides are eluted from the surfaces, their DNA is extracted and sequenced. Some examples of the sequences consist of noble metals (Pt, Pd, Ag, Au), oxides (ZnO, Al_2O_3, SiO_2), semiconductors (GaN, Cu_2O, TiO_2, ITO, sulfides, selenides) and other materials (mica, graphite, calcite). Typically 50 or more peptides are selected for any given inorganic material with different level of binding strengths. These peptides can be referred as the first set of selected peptide sequences from an initial random library screening. Since in natural evolution, a similar process is improved after reoccurring cycles of mutations and selection, similarly selected peptides can be subjected to another cycle of selection, which is called the construction of a second-generation combinatorial library. In the second selection procedure, neighboring residues are randomized and selection is carried out accordingly to find stronger binders showing a high degree of specificity for one material [67, 68].

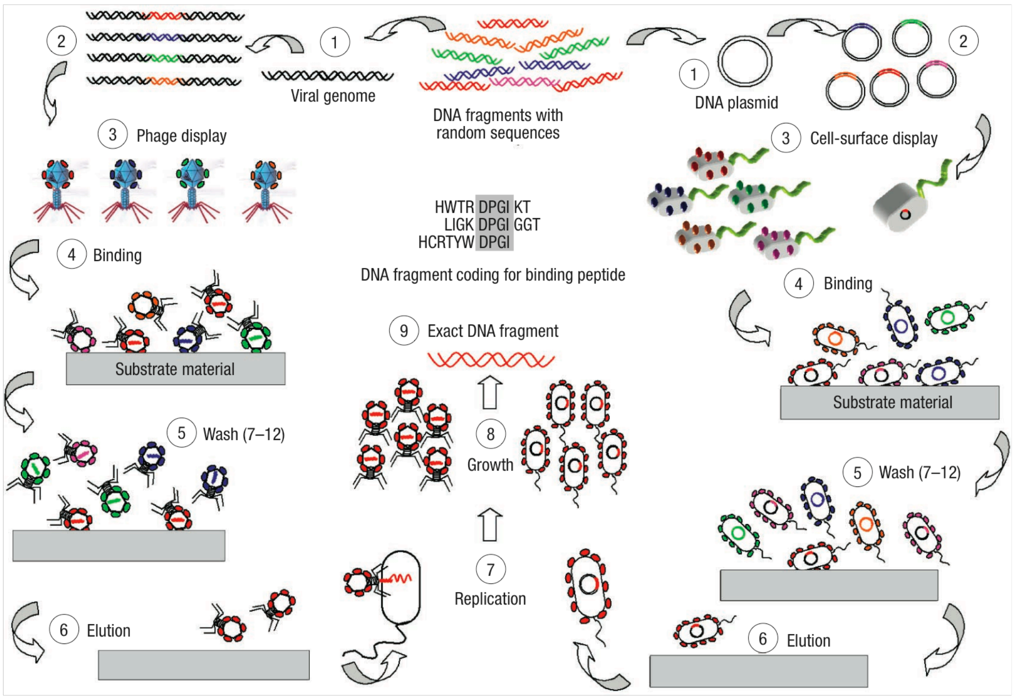

Figure 4.1 Schematics showing phage display and cell-surface display techniques [64].

After selection procedure, sequences are compared for their similarity scores using genetic algorithm procedures. BLOSUM-like matrix, which is typically used for comparing the protein sequences of different organisms, is utilized. The principle of the matrix is based on a optimization in which peptides with similar binding properties for a certain material have a very high score and those with different binding properties have a low score. It also depends on the assumption that peptides having a remarkable match to a known binder are expected to bind with high affinity to that [67, 68].

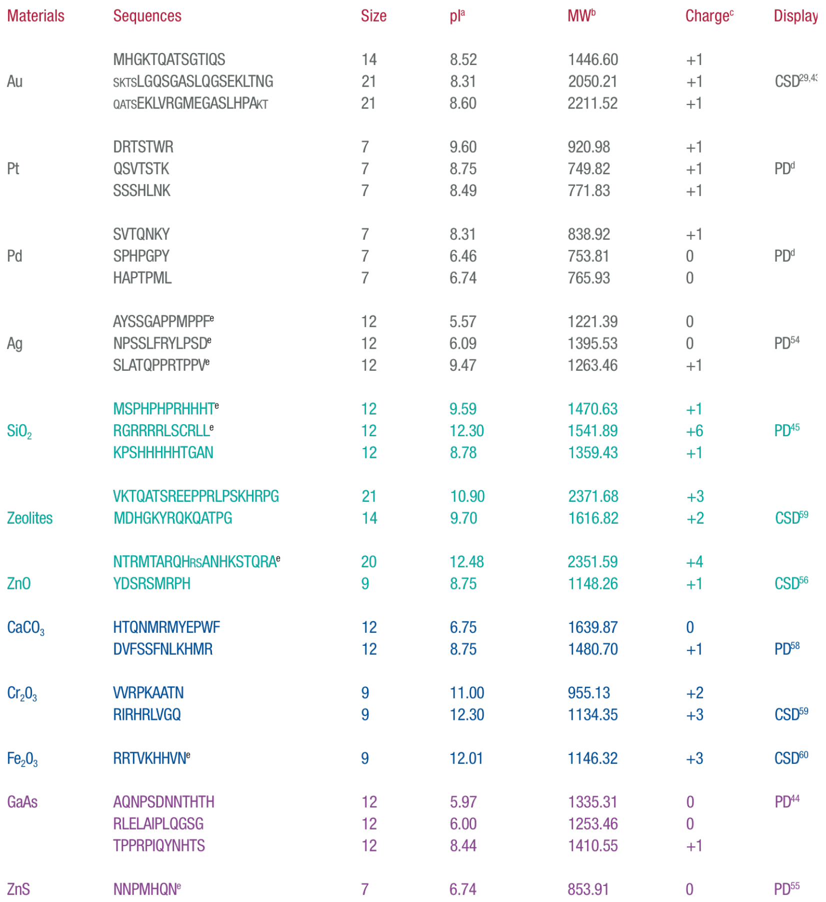

Materials	Sequences	Size	pI[a]	MW[b]	Charge[c]	Display
Au	MHGKTQATSGTIQS	14	8.52	1446.60	+1	CSD[29,4
	SKTSLGQSGASLQGSEKLTNG	21	8.31	2050.21	+1	
	QATSEKLVRGMEGASLHPAKT	21	8.60	2211.52	+1	
Pt	DRTSTWR	7	9.60	920.98	+1	PD[d]
	QSVTSTK	7	8.75	749.82	+1	
	SSSHLNK	7	8.49	771.83	+1	
Pd	SVTQNKY	7	8.31	838.92	+1	PD[d]
	SPHPGPY	7	6.46	753.81	0	
	HAPTPML	7	6.74	765.93	0	
Ag	AYSSGAPPMPPF[e]	12	5.57	1221.39	0	PD[54]
	NPSSLFRYLPSD[e]	12	6.09	1395.53	0	
	SLATQPPRTPPV[e]	12	9.47	1263.46	+1	
SiO_2	MSPHPHPRHHHT[e]	12	9.59	1470.63	+1	PD[45]
	RGRRRRLSCRLL[e]	12	12.30	1541.89	+6	
	KPSHHHHHTGAN	12	8.78	1359.43	+1	
Zeolites	VKTQATSREEPPRLPSKHRPG	21	10.90	2371.68	+3	CSD[59]
	MDHGKYRQKQATPG	14	9.70	1616.82	+2	
ZnO	NTRMTARQHRSANHKSTQRA[e]	20	12.48	2351.59	+4	CSD[56]
	YDSRSMRPH	9	8.75	1148.26	+1	
$CaCO_3$	HTQNMRMYEPWF	12	6.75	1639.87	0	PD[58]
	DVFSSFNLKHMR	12	8.75	1480.70	+1	
Cr_2O_3	VVRPKAATN	9	11.00	955.13	+2	CSD[59]
	RIRHRLVGQ	9	12.30	1134.35	+3	
Fe_2O_3	RRTVKHHVN[e]	9	12.01	1146.32	+3	CSD[60]
GaAs	AQNPSDNNTHTH	12	5.97	1335.31	0	PD[44]
	RLELAIPLQGSG	12	6.00	1253.46	0	
	TPPRPIQYNHTS	12	8.44	1410.55	+1	
ZnS	NNPMHQN[e]	7	6.74	853.91	0	PD[55]

Figure 4.2- Showing examples of peptide sequences having affinity for different types of inorganic materials [64].

4.3 Stability tests of genetically engineered peptides for inorganics

in previous studies of our collaborators, surface plasmon resonance (SPR) experiments were done using a configuration and experimental method mentioned [69]. SPR measurements were carried at 27 ± 0.1 ^{o}C using a temperature controller system. The solutions used in these experiments were flowed through the apparatus using a peristaltic pump (80 µL/min), and switching between different solutions was achieved via the use of a 6-port valve (Upchurch Scientific). To establish a baseline for experimental measurements, solutions containing buffer alone were first flowed through the apparatus and coated slide. Next, buffer solutions containing each peptide (0.7, 1.7, 5.1 μM final peptide concentrations) were introduced. After a specified interval to allow peptide adsorption onto the silica thin films, a solution consisting of buffer minus peptide was flowed through the system to monitor peptide desorption from the target thin film. The SPR data were collected using WinSpectral 1.03 software, which measures the normalized dip spectrum at periodic intervals (Figure 4.3). This dip is fitted to a 4th degree polynomial function for generating the time-dependent metric sensogram. The conventional Au SPR substrate was coated with 10 nm of silica layer on top of the Au; each of the experiments was carried out at using a slide only for one time. The calculation of the adsorption of bio-QBP1 on silica surface was made using a modified Langmuir adsorption models. The details of the calculation that adsorption isotherms from the experimental data are the same as the associated section in Chapter 6.1.

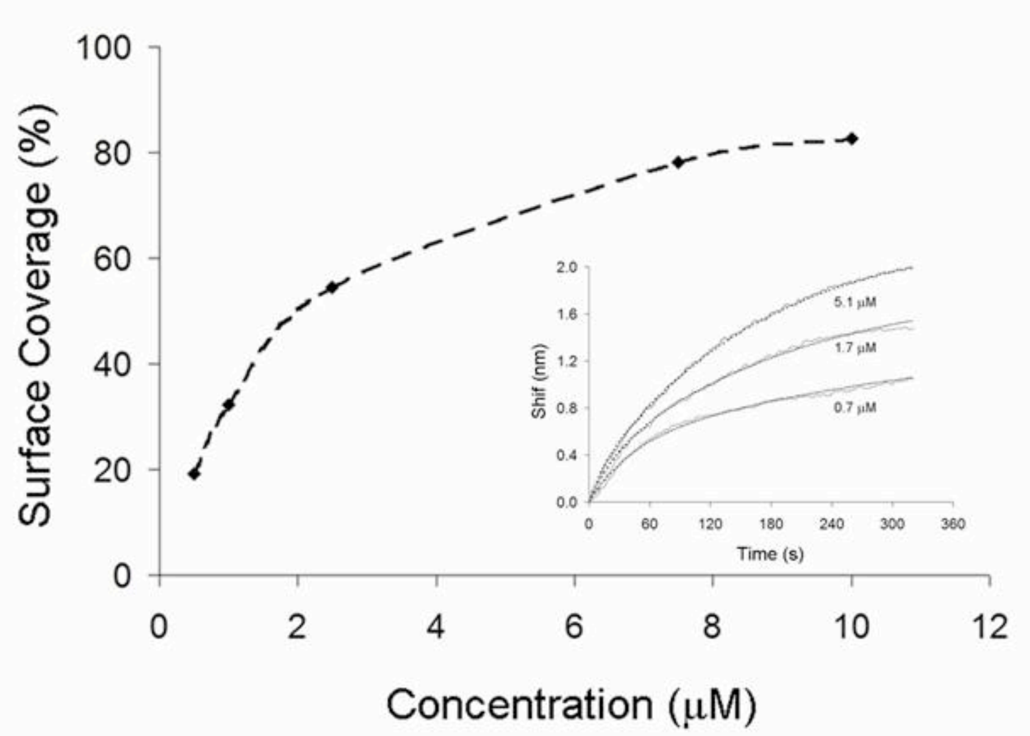

Figure 4.3 – Surface coverage of quartz binding peptide (QBP1) as a function of different concentrations

Chapter 5

White light emitting diodes

5.1 Overview of light emitting diode (LEDs)

A light emitting diode consists of a semiconductor doped with impurities to form a p-n junction. In a standard LED, by driving a forward current through its metal contacts between n-type and p-type semiconductors, electrons and holes are injected into the semiconductor and recombination of electrons and holes gives rise to emission of light by spontaneous emission in every direction and coupled out through its optical emission cone determined by the ratio of the refractive indices of its semiconductor to air. The wavelength of the light emitted, and therefore its color, is determined by the band gap energy of the materials forming the p-n junction. Direct band gap materials with energies corresponding to near-infrared, visible or near-ultraviolet ranges are typically used. LEDs are usually built on an n-type substrate, with an electrode attached to the p-type layer deposited on its surface. Many commercial LEDs, especially GaN/InGaN, also use sapphire substrate [70].

The light from an LED is generally coupled into a much lower-index medium since the refractive index of most LED semiconductor materials is quite high. The large index difference makes the total internal reflection quite considerable and the produced light gets partially reflected back into the semiconductor, where it may be absorbed and turned into additional heat; this is usually one of the major causes of LED inefficiency. Often more than half of the emitted light is reflected back at the LED-package and package-air interfaces. The reflection is most commonly reduced by using a package with the diode in the center so that the outgoing light rays hit the surface perpendicularly, at which angle the reflection is minimized. Substrates that are transparent to the emitted wavelength, and backed by a reflective layer, increase the LED efficiency. The refractive index of the package material should also match the index of the semiconductor, to minimize back-reflection. An anti-reflection coating may be added as well [70].

LEDs have many advantages such as they generate more light per watt than incandescent bulbs; this is practical in battery powered or energy-saving devices. They can emit light of an desired color without the use of color filters that traditional lighting methods require. This is more efficient and can lower initial costs. The solid package of the LED can be designed to focus its light. Incandescent and fluorescent sources often require an external reflector to collect light and direct it in a usable manner. LEDs light up very quickly. A typical red indicator LED will achieve full brightness in μs. At the same time they can have a relatively long useful life. LEDs, being solid state components, are difficult to damage with external shock, unlike fluorescent and incandescent bulbs which are fragile. LEDs can be very small and are easily populated onto printed circuit boards and do not contain mercury, unlike compact fluorescent lamps. On the other hands, use of LEDs has some disadvantages as well. LEDs are currently more expensive than more conventional lighting technologies because of low lumen output, the drive circuitry and power supplies needed. However, when considering the total cost including energy and maintenance costs, LEDs are far better than incandescent or halogen sources. LED performance largely depends on the ambient temperature of the operating environment. Over-driving the LED in high ambient temperatures may result in overheating of the LED package, eventually leading to device failure. Sufficient heat-sinking is required to maintain long life. This is especially important in automotive, medical, and military applications where the device must operate over a large range of temperatures. The spectrum of some white LEDs differs significantly from a blackbody radiator, such as the sun or an incandescent light. The point at 460 nm and dip at 500 nm can cause the color of objects to be perceived differently under LED illumination than sunlight or incandescent sources, due to metamerism [70].

5.2 White light emitting diodes

There are two ways of producing high intensity white-light using LEDs. One is to use individual LEDs that emit three primary colors – red, green, and blue, and then mix all the colors to produce white light. The other is to use a phosphor or another luminescence material to convert monochromatic light from a blue or UV LED to broad-spectrum white light [70].

White light can be produced by mixing differently colored light, the most common method is to use red, green and blue (RGB). Hence the method is called multi-colored white LEDs because its mechanism is involved with complicated electro-optical design to control the blending and diffusion of different colors, this approach has rarely been used to mass produce white LEDs in the industry. There are several types of multi-colored white LEDs: di-, tri-, and tetrachromatic white LEDs. Several key factors that play among these different approaches include color stability, color rendering index, and luminous efficacy. Often higher efficacy will mean lower color rendering, presenting a trade off between the luminous efficiency and color rendering [70].

The other type of LEDs is color conversion LEDs. The operating principle of color conversion LEDs depends on using luminophores integrated on top of a blue or near-UV emitting LED. The electroluminescence of LED optically pumps the luminophores on the LED and then both electroluminescence of LED and photoluminescence of luminophores contribute to white light generation.

Phosphors, dye polymers or nanocrystals can be used as luminophores in white light emitting diodes [70].

5.2.1 Phosphor based while light emitting diodes

This method involves coating a LED of one color (mostly blue LED made of InGaN) with phosphor of different colors to produce white light; the resultant LEDs are called phosphor based white LEDs. Depending on the color of the original LED, phosphors of different colors can be employed. If several phosphor layers of distinct colors are applied, the emitted spectrum is broadened, effectively increasing the color rendering index (CRI) value of a given LED.

Although phosphor based LEDs have a lower efficiency then normal LEDs due to the heat loss and also other phosphor-related degradation issues, it is still the most popular technique for manufacturing high intensity white LEDs. This is because the design and production of a light source or light fixture is much simpler than, for instance, a complex RGB system.

The largest issue for the efficacy is the seemingly unavoidable energy loss. However, much effort is being made on optimizing these devices to higher light output and higher operation temperatures. The efficiency can, for instance be increased by adapting better packaging design or by using more suitable types of phosphors.

Technically the phosphor based white LEDs encapsulate InGaN blue LEDs inside of a phosphor coated epoxy. A common yellow phosphor material is cerium-doped yttrium aluminium garnet (Ce3+:YAG).

White LEDs can also be made by coating near ultraviolet (n-UV) emitting LEDs with a mixture of high efficiency europium-based red and blue emitting phosphors plus green emitting copper and aluminium doped zinc sulphide (ZnS:Cu, Al).

Today, the most commonly used solid state lighting sources are based on the integration of yttrium aluminium garnet YAG phosphors on blue InGaN/GaN light emitting diodes LEDs. The broad yellowish emission of YAG phosphors along with blue LED yields white light generation with correlated color temperatures of 4000-8000 K, corresponding to the neutral-and cool-white intervals, and color rendering indices typically lower than 80. However, especially for wide- scale use in indoor illumination applications, white LEDs are required to provide warm enough color temperature smaller then 4000 K with high enough color rendering index greater than 80 [70].

5.2.1 Dye and Polymer Based WLEDs

There is also dye and polymer based WLEDs. Even though Coumarin 6 is a dye with very high quantum efficiency, since its quantum efficiency drastically drops after certain amount of photon emission, it is not feasible to use it commercial WLED. Similarly polymer based WLEDs suffers from the long term stability problems while it may be a better candidate for lighting applications than phosphorus because of its low cost and strong absorption in near UV [70].

5.3 Nanocrystal based hybrid LEDs

5.3.1 Operating principle

Nanocrystal emitters are particularly advantageous for use in white light sources because they feature tunable and relatively narrow emission across the visible spectral range and small overlap between their emission and absorption spectra, and also provide the ability to be easily and uniformly deposited in solid films with common techniques e.g., spin casting and dip coating.

To operate a nanocrystal based hybrid white light emitting diode, LED operates as the pump the integrated quantum dots, which are used for their photoluminescence sources as a luminophors. Electroluminescence of LED and photoluminescence of quantum dots are collected to contribute together to generation of white light. With the correct color choice of quantum dots and the corresponding LED emission wavelength, emission of nanocrystal based white light emitting diodes covers a wide range of spectrum from blue to red with sufficient spectral power distribution, owing to the fact that nanocrystals having tunable emission wavelength with changing sizes. As expected, optical parameters of generated white light are dependent on thickness, density, type, and order of quantum dots. The order of different types of quantum dots affects reabsorbtion of photons emitted from LED by next layer of nanocrystals. All these parameters determine the color properties (tristimulus coordinates, correlated color temperature and color rendering index) of the generated white light by adjusting the device parameters to determine which spectral intervals of the visible spectrum would contribute to white light [70].

5.3.1 CdSe/ZnS Nanocrystals Hybridized on blue InGaN/GaN LEDs

We can give two examples of CdSe/ZnS nanocrystal hybridized with blue LED or near-UV LED from previous studies of our group. In the study of CdSe/ZnS core shell nanocrystals integrated with blue LED, an InGaN/GaN LED with emission peak at 440 nm was used. Fulfil the requirements of white light generation, yellow nanocrystals with emission peak at 580 nm was chosen to be integrated by means of the host polymer (PMMA). When the parameters were calculated from the emission spectra of the overall structure, it was found that tristimulus coordinates x = 0.37 and y = 0.25, a color rendering index 14.6 and color temperature 2692 K which corresponds to white regime in the CIE 1931 chromaticity diagram.

Another example is based on using two types of nanocrystals with blue InGaN/GaN LEDs (440 nm). First 500 nm cyan emitting CdSe/ZnS coreshell nanocrystals were placed on blue emitting LED and then 620 nm red emitting CdSe/ZnS coreshell nanocrystals were placed on cyan nanocrystal layer. The emission spectra is fall in white region with x = 0.37, y = 0.28, color rendering index of 19.6 and color temperature of 3246 K. It is notable that with using two types of nanocrystals it is possible to improve color rendering index. In this case, it is improved from 14.6 to 19.6.

Given that hybridizing dual combinations of CdSe/ZnS coreshell nanocrystals improved color rendering index, using three distinct type of nanocrystals further enhanced the color rendering index of generated white light. First, green (540 nm), then yellow (580 nm) and finally red (620 nm) emitting quantum dots were placed on top of the blue emitting (440 nm) InGaN/GaN LED so that reabsorbtion of emitted photons in each level was avoided. Eventually, the operating point was in white regime with parameters x = 0.30, y = 0.28, color rendering index of 40.9 and color temperature of 7521 K.

Furthermore with quadruple integration of green (540 nm), cyan (500 nm), yellow (580 nm), and red (620 nm) CdSe/ZnS coreshell nanocrystals with blue emitting (440 nm) InGaN/GaN LED, x = 0.24, y = 0.33, color rendering index of 71.0 and color temperature of 11171 K were achieved which gives an operating region in white regime and with highly improved color rendering index due to the multi-hybridization of green, cyan, yellow and red emitting nanocrystals with the blue LED.

5.3.2 Layer-by-layer assembly of CdSe/ZnS nanocrystals hybridized on n-UV LEDs

Another design which was previously studied in our group is hybrid white light sources based on layer-by-layer assembly of nanocrystals on n-UV emitting diodes. Layer-by-layer use of cyan (504 nm) and red (615 nm) CdSe/ZnS nanocrystals on n-UV led to the operating point of x = 0.37, y = 0.46, color rendering index of 43.1 and color temperature of 4520 K in near-white region and using cyan (504 nm), yellow (580 nm) and red (615 nm) emitting nanocrystals resulted emission again in white region with the parameters x = 0.24 and y = 0.33.

In the integration of three different nanocrystals, we utilized cyan (504 nm), yellow (580 nm) and red (615 nm) CdSe/ZnS nanocrystals on n-UV LED with the order of cyan was first placed on LED, yellow and red were put on top of cyan respectively with 23 % NC-to-PMMA volume ratio. The resulting operation region is x = 0.38, y = 0.48, color rendering index of 67.6 and color temperature of 4434 K improved color rendering index with respect to two nanocrystal case.

In such devices, when we compared the performance with blue InGaN/GaN LEDs, it is more advantageous to use n-UV LED in WLED design for a number of reasons. Primarily, with higher energy optical pumping, it is possible to get same results with thinner nanocrystal films with n-UV LEDs. Also, using n-UV light makes the white emission depends only on the emission originating from nanocrystals since n-UV light of LED does not contribute to the visible range of the emission spectra; therefore, it becomes possible to easily tune the visible range only with nanocrystal emissions. Optical power of UV LEDs is supposed to improve significantly in near future which would give rise to widespread use of UV LEDs in many complex device fabrication.

Sample #	Hybridized nanocrystals	LED λ_{EL} (nm)	Concentration (μmol ml^{-1})	x	y	T_c (K)	R_a
1	—	452	—	0.14	0.03	34 367	−51.5
2	Y	452	2.36	0.15	0.04	34 367	−40.2
3	Y	452	2.36	0.16	0.06	34 367	−28.6
4	Y	452	2.36	0.20	0.10	34 366	−10.1
5	Y	452	2.36	0.24	0.13	34 366	−3.8
6	Y	452	2.36	0.43	0.28	1 882	15.8
7	G, Y	452	5.59, 2.36	0.44	0.29	1 989	37.5
8	G, Y	452	5.59, 2.36	0.45	0.33	2 165	54.5
9	G, Y	452	5.59, 2.36	0.52	0.37	1 754	50.2
10	R, Y	452	0.88, 2.36	0.57	0.30	1 121	42.2
11	R, Y	452	0.88, 2.36	0.62	0.30	1 000	50.7
12	C, Y	452	12.05, 2.36	0.24	0.13	34 366	−3.4
13	C, Y	452	12.05, 2.36	0.36	0.23	2 651	32.4
14	C, Y	452	12.05, 2.36	0.36	0.27	3 228	48.3
15	C, Y	452	12.05, 2.36	0.42	0.31	2 311	50.2
16	Y	440	0.11	0.37	0.25	2 692	14.6
17	C, Y	440	0.37, 0.11	0.37	0.28	3 246	19.6
18	G, Y, R	452	0.27, 0.11, 0.025	0.30	0.28	7 521	40.9
19	C, G, Y, R	452	0.37, 0.27, 0.1, 0.025	0.24	0.33	11 171	71.0
20*	C, Y, R	452	2.54, 0.19, 0.06	0.44	0.26	1 625	38.8
21	C, Y, R	452	2.8, 2.8, 2.8	0.20	0.10	34 366	1.9
22	C, Y, R	383	2.8, 2.8, 2.8	0.51	0.39	1 979	71.9
23*	C, Y, R	383	2.54, 0.19, 0.06	0.61	0.36	1 238	74.3
24	C, R	452	2.8, 2.8	0.20	0.11	34 367	4.0
25*	C, R	452	2.73, 0.06	0.24	0.13	34 366	−13.8
26*	C, R	383	2.73, 0.06	0.57	0.37	1 477	47.6
27	C, R	383	2.8, 2.8	0.52	0.41	1 977	42.1

Table 5.1- Hybrid NC-WLED sample characteristics. (C: cyan NC; G: green NC; Y: yellow NC; R: red NC; * means blended NC hybridization.)

5.3.3 Tuning color parameters of white light both in blue and n-UV LEDs

In this study we present nanocrystal-based warm-white hybrid light sources with high color rendering index that incorporate the right color-converting combinations of green and red CdSe/ZnS core-shell nanocrystals emitting at 555 nm and 613 nm, respectively hybridized on blue InGaN/GaN light emitting diodes at EL at 452 nm. The use of such quantum dot emitters makes possible to accomplish high correlated color temperature at the same time while sustaining the chromaticity operating point within the white region and persisting high color rendering index. This is mainly because nanocrystals have comparatively narrow emission in the visible e.g., with a full width at half maximum of 30 nm in solution, and their peak emission wavelength can be precisely tuned with the size effect as necessary. As a result, using a right color-converting combination of nanocrystals, it is possible in principle to generate and adjust any emission spectrum as desired. We develop and demonstrate three sets of proof-of-concept warm-white LEDs with high-quality white light properties.

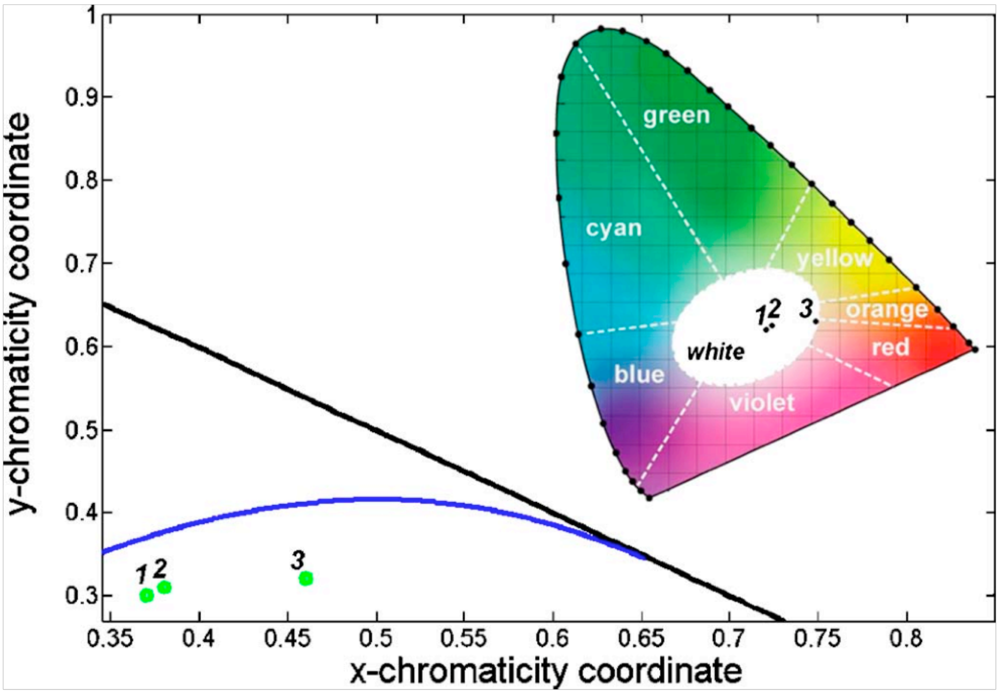

Figure 5.1- CIE chromaticity diagram zoomed-in for the loci of the tristimulus coordinates of

our nanocrystal-hybridized warm-white light emitting diodes green points along with the planckian locus blue line. A complete CIE 1931 chromaticity diagram is also given with the tristimulus coordinates of our hybrid warm-white light emitting diodes in the inset.

To make the hybrid warm-WLEDs, we integrated green and red emitting CdSe/ZnS core-shell nanocrystals at 555 nm and 613 nm, respectively in the PMMA matrix on top of the blue LEDs. To obtain white light generation with warm color temperature and high color rendering index, we analyze the blackbody radiators which are used as the reference sources and figured out the correct amount of NC emitters for the LED hybridization to achieve high performance.

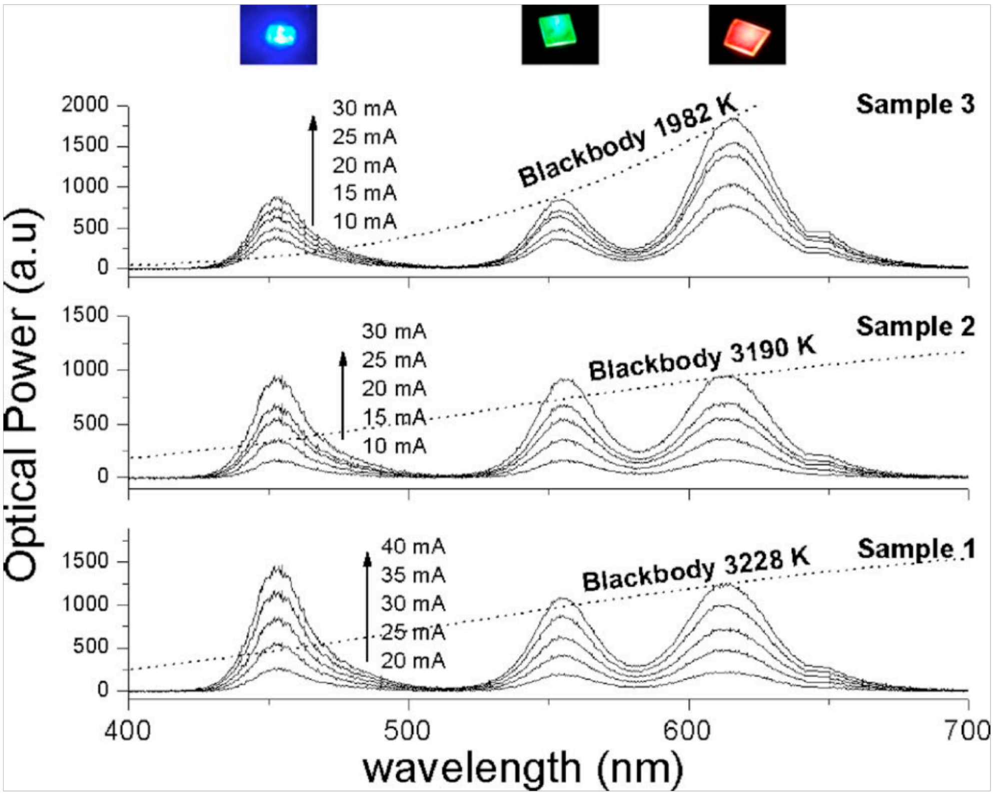

Figure 5.2- Luminescence spectra of the nanocrystal hybridized warm-white light emitting diodes (samples 1–3).

As the color temperature of the radiators decreases getting warmer in color, the red part in the visible becomes more dominant. Therefore, to achieve warmer color temperatures, we increase the red luminescence in the visible spectrum, while maintaining the chromaticity point in the white region and sustaining high color rendering index.

In the first experiment, for their hybridization on blue LED EL 452 nm, we design to incorporate 0.22 mg 0.578 nmol of red-emitting CdSe/ZnS core-shell nanocrystals and subsequently 0.26 mg 2.166 nmol of green-emitting nanocrystals. On the other hand, the green nanocrystal emitters are chosen to balance out the red emission conveniently at 555 nm along with the blue LED emission at 452 nm and, consequently, keep the operating chromaticity coordinates within the white region and the color rendering index high enough. The emission of the LED leads to x = 0.37, y = 0.30, luminous efficacy of optical radiation 307 lm/W, color rendering index of 82.4, and color temperature index of 3228 K corresponding to a warm-white LED with a high color rendering index of 82.4

For the second demonstration, we design to integrate 0.13 mg 1.083 nmol of green-emitting CdSe/ZnS core-shell nanocrystals 555 nm and then 0.44 mg 1.156 nmol of red-emitting nanocrystals 613 nm on the top of blue LED 452 nm. This implementation experimentally leads to x = 0.38, y = 0.31, luminous efficacy of optical radiation of 323 lm/W, color rendering index of 81.0, and color temperature of 3190 K. Here, the tristimulus coordinates shift to the red side of the CIE chromaticity diagram and the correlated color temperature decreases to 3190 K because of the increased relative intensity of the red-emitting nanocrystals. Therefore, this light source achieves a warmer-white light generation while maintaining its operation in white. The color rendering index slightly drops to 81.0, which still satisfies the criterion for the future solid stated light sources, and the luminous efficacy of optical radiation reaches a relatively high value of 323 lm / W.

Sample	x	y	LE (lm/W)	CRI	CCT (K)
1	0.37	0.30	307	82.4	3228
2	0.38	0.31	323	81.0	3190
3	0.46	0.32	303	79.6	1982

Table 5.2- Optical properties of our nanocrystal hybridized warm-white light emitting diodes

As the last demonstration, we design to hybridize 0.13 mg 1.083 nmol of green-emitting CdSe/ZnS core-shell nanocrystals 555 nm and 0.66 mg 1.734 nmol of red-emitting nanocrystals 613 nm on the blue LED 452 nm. The resulting emission spectra corresponds to x = 0.37, y =0.30, luminous efficacy of optical radiation of 303 lm/W, color rendering index of 79.6, and color temperature of 1982 K. This operating point stands approximately on the boundary of white region near to the red-color end. Therefore, this hybrid white LED generates highly warm-white light at an extra low correlated color temperature of 1982 K.

Hybridizing CdSe/ZnS core-shell NC emitters on InGaN/GaN based blue LEDs, we demonstrate three warm-white light sources with color temperature ranging from 3227 to 1982 K. In demonstrations, the color rendering indices as high as 82.4 and luminous efficacies of optical radiation as high as 327 lm/W are also achieved.

Chapter 6

Our targeted-self assembly of quantum dot light emitters on LEDs by using peptides as smart molecular linkers

6.1 Conventional method vs. our innovative approach for immobilization of nanocrystal quantum dots emitters

During this study, we utilized quartz binding peptide 1 (QBP1) as a smart molecular linker for quantum dot (Q-Dot) assemblies first on a single material surface, which is quartz (fused silica), and subsequently, on the targeted specific regions of multi-material chips and real optoelectronic devices such as light emitting diodes (LEDs). Our peptides were tagged with one biotin molecule per peptide at the N terminus and thus, biotinylated QBP1 (bio-QBP1, in short) were obtained. This allowed (bio-QBP1) to exhibit hetero-bifunctional property, both employing their silica binding property and coupling with streptavidin binding molecules on the other ends. To build self-assembled layers of Q-Dots on the silica surface, we investigated the conventional approach of sequentially laid layers of peptides and Q-Dots.

Conventional method relies on assembling different materials, including GEPIs, quantum dot emitters and other nanoparticles as a layer on top of each other on a substrate. This is a very common method used both in study of new nanostructures and in standard fabrication method of many layered architectures such as nanocrystal hybridized white light emitting diodes as described in the previous chapter.

In our work, first bio-QBP1 was dissolved in a tris buffered saline (abbreviated TBS) solution to obtain 100 μg/ml final peptide concentration. TBS is used to sustain pH level of biochemical solutions within a comparatively limited range. TBS solution used in out experiments contains 200 mM NaCl, 45 mM Na_2CO_3, and 55 mM KH_2PO_4. To test if the concentrations of NaCl, Na_2CO_3 and KH_2PO_4 are optimal for the best binding capacity of our QBP1s, we varied salt concentrations, for example, for 200 mM, 400 mM, 800 mM, and 1600 mM. We consequently found the concentration of 200 mM as the optimum value. Moreover, in this study, the pH level of our TBS was adjusted with HCl at 7.4.

We immobilized our peptides by drop casting them on polished 7 mm by 7 mm pre-cut quartz surfaces, which we previously cleaned in acetone, isoproponal, and deionized water in turn ultrasonic bath for 5 minutes each. Then, our samples were incubated for minimum 2 hours in a vapor chamber to prevent desiccation during the incubation by maintaining constant vapor level. The non-specifically bound and unbound peptides were further removed from the surface by excess washing with TBS solution from the quartz surface. At this stage, the bio-QBP1 decorated surface was ready for the assembly of the additional streptavidin (SA) conjugated Q-Dots (SA-Q-Dots). Water soluble SA-Q-Dots were purposely chosen instead of non-functionalized Q-Dots or other ligand or antibody conjugated Q-Dots since SA exhibits extremely strong affinity for the biotin. The biotin-streptavidin complex has a low dissociation constant, K_d (on the order of $4x10^{-14}$ M), which is an equilibrium constant used in chemistry and biochemistry to gauge the tendency of a big complex structure to dissociate reversibly into its smaller parts or molecules. The SA-biotin conjugation leads to one of the strongest non-covalent biological interactions known in nature. Our SA-Q-Dots (Evident Tech.) provided peak emission wavelengths at 520 nm (adirondack green) and 620 nm (maple red-orange). These Q-Dots are conjugated to PEG (polyethylene glycol) lipids, with hydrodynamic diameter of approximately 25 nm. These Q-Dots are then activated with streptavidin molecules later to couple with biotin. Approximately, one SA-Q-Dot contains 5 to 10 streptavidin molecules on its surface and its hydrodynamic diameter can increase up to 40 nm. Taking into consideration of 4 biotin binding sites in a single SA molecule, SA-Q-Dot and bio-QBP1 concentrations and related volumes were adjusted such that bio-QBP1 would have sufficiently high surface coverage (see SRP experiments, Figure 4.3 and 6.2) and there would be adequate amount of SA-Q-Dots interacting with bio-QBP1. Therefore, we used 100 μg/ml bio-QBP1 and 2.5 μM SA-Q-Dot in equal volumes (15-30 μl) per quartz substrate. Subsequently, SA-Q-Dots were layered on the bio-QBP1 film by drop casting. The same washing procedure was applied to the assembled SA-Q-Dot layers to satisfy the conditions for a stable and homogenous Q-Dot film. A negative control group was also prepared by assembling the SA-Q-Dot layer directly on silica surface, in the absence of bio-QBP1 film hybridized on the surface.

The photoluminescence (PL) measurements of these samples and their control groups were taken with Jobin Yvon Traix 550 CCD photoluminescence system with HeCd laser emitting at 325 nm, 2000 μm slit width and 2000 ms integration time at room temperature in a dark room. The results of these photoluminescence measurements, however, surprisingly indicated that the samples are not statistically much more better than their negative control groups and the optical behavior of the samples is not reproducible. In Figure 6.1, the variation in the fluorescence image of the SA-Q-Dots on the silica surface exhibits a non-homogenous spreading of the SA-Q-Dots, which shows some of the regions on the chip to exhibit as low photoluminescence as the negative control group. This observation points out that diffusion is limited for these Q-dots dropped on the peptide film during their self-assembly process. In this case, bio-QBP1 functionalized silica surface contains a large number of biotin that may get stuck on the surface, but the streptavidin must be able to get in contact with the biotin on the surface by diffusion to assemble the SA-Q-Dots on the surface. Thus, this means the interaction of SA-Q-Dots and surface biotin is mass transfer limited, as there is no further mixing during the drop casting process.

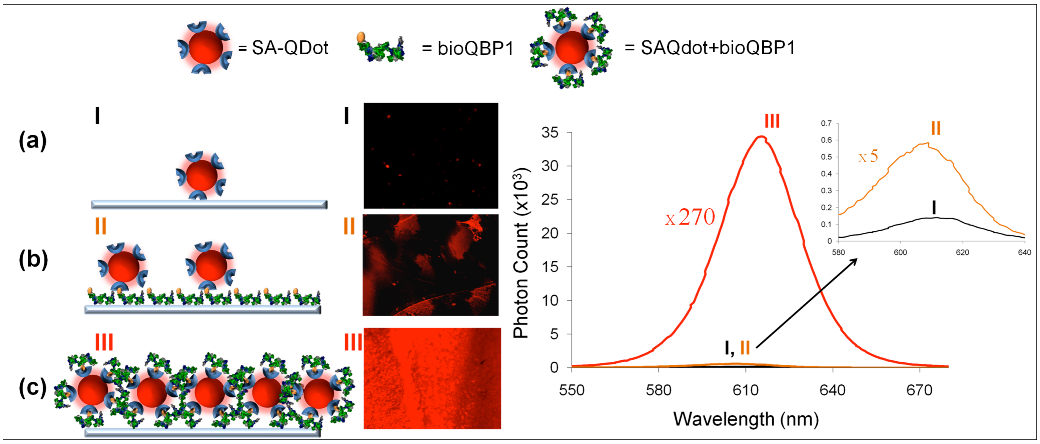

Figure 6.1 - The targeted self-assembly of quantum dots (Q-Dots) (emitting in red at 610 nm) on silica surfaces. (a) For the negative control group, only streptavidin conjugated quantum dots (SA-Q-Dots) were dropped on silica surface (without using any GEPI) and then they were washed to remove non-specifically interacting ones. Only very few red SA-Q-Dots remained on the silica surface. (b) Using conventional approach, after the decoration of the silica surface with biotinylated silica binding peptide (bio-QBP1), the same SA-Q-Dots were dropped on the modified surface and then were washed to remove the unbound ones. Such sequential incubation of first peptides and then SA-Q-Dots repeatedly resulted in non-homogenous films. (c) In our approach, the same SA-Q-Dots were first conjugated in solution with silica binding peptide (bio-QBP1) by means of the streptavidin-biotin interaction, and then bio-QBP1 decorated SA-Q-Dots were assembled on the silica surface and washed to remove the unbound specifies. Such hybrid QBP1-Q-Dot nanoassembly approach reproducibly led to uniform films of quantum dots with increased density on the silica surface. In each case (a)-(c), the florescence microscopy images of the assembled quantum dots are shown along with the corresponding photoluminescence spectra. The photoluminescence spectra for all cases (a), (b), and (c) are represented on the graph, with the inset showing a zoom-in at low intensity levels for (b) and (c). Compared to the negative control group (a), the conventional approach (b) led to 5 fold improvement, while the

innovative approach (c) resulted in ~270 fold improvement in the peak emission of bound quantum dots, demonstrating that the innovative approach is 54 times better than the conventional one.

To overcome this problem, in our innovative approach, the SA-Q-Dots were first blended with bio-QBP1 and brought in contact in the buffer solution before incubation on the silica surface. We calculated and optimized the concentration and volume ratio of bio-QBP1 and SA-Q-Dots so that the surface of SA-Q-Dots would be fully decorated with bio-QBP1 taking into account of that there are 5 to 10 SA molecules per Q-Dot and 4 biotin binding sites per SA molecule. The resulting peptide hybridized Q-Dots, or hybrid nanoassemblies, can easily bind to quartz surface because of their special structure with binding peptides fully decorating the quantum dot in three dimensions. Similar to the conventional method, quartz substrates were cleaned with the same procedure and equal volumes (15-30 μL) of 100 μg/ml bio-QBP1 and 2.5 μM SA-Q-Dots were used for each quartz chip and the final solution was gently mixed in vortex mixer around 500 rpm. Blending SA-Q-Dots and bio-QBP1 prior to drop casting and the high degree of affinity between SA and biotin helped efficient decoration of SA-Q-Dots with the bio-QBP1, as well as increasing interactions between biotin and streptavidin. Then the resulting hybrid bio-QBP1-SA-Q-Dots nanoassemblies were incubated on the surface of the silica and the non-specifically bound and unbound ones were removed by the described washing procedure and were finally dried with nitrogen gun. All these experiments were also coupled with a negative control group experiment. In our approach, we observed a significant enhancement in the photoluminescence intensity and sufficient uniformity of the peptide-assisted assembly of the QBP1-Q-Dots on silica surface. Figure 6.1 shows fluorescence microscopy (FM) images of homogeneous Q-Dot film formation, along with strong photoluminescence. The samples prepared by the innovative approach show 270 times stronger peak photoluminescence intensity compared to the negative control groups. On the other hand, the conventional approach led to only 5 times stronger photoluminescence intensity, compared to the negative control group. This demonstrates that our approach is 54 times better than the conventional method.

Bio-QBP1 assisted Q-Dot immobilization on silica surface by means of conventional and innovative approaches were also monitored through surface plasmon resonance (SPR) spectroscopy and quartz crystal microbalance with dissipation (QCM-D) monitoring experiments. SPR experiments are based on excitation of surface plasmons by light and widely used for measuring adsorption of a material on Au surface though a flow cell. Similarly, in our case SPR experiments were fulfilled to determine the binding kinetics of SA-Q-Dots on silica surface in the conventional method, our approach, and the negative control group. In other words, we investigated intermolecular interactions between bio-QBP1 decorated silica surface and SA-Q-Dots in the conventional method. In similar fashion, we studied intermolecular interaction between bio-QBP1 hybridized SA-Q-Dots and silica surface in our approach. Likewise, intermolecular interactions between SA-Q-Dot and silica surface were observed in negative control groups.

To prepare conventional Au SPR slides, first glass substrates were cleaned by successively keeping in ultrasonic bath of acetone, isoproponal, and deionized water for 5 minutes each. To firmly adhere Au layer on glass, first 3 to 5 nm thick Ti layer and then 45 nm thick Au were deposited with thermal evaporator (LH Leybold AG, IC/4 Plus Inficon Deposition Controller). Next, 10 nm of silica layer was deposited on top of Au layer with plasma enhanced chemical vapor deposition technique (PECVD) (Plasma Technology Plasmalab MicroP) at 250 ^{o}C. The substrates were used only in one time during the experiment.

The SPR experiments were carried out with a dual-channel instrument using Kretschmann configuration. In Kretschmann configuration, surface plasmons are excited by light coming from the glass side and the evanescent waves pervade to the other side of metal film, which is evaporated on the glass slide. The SPR instrument consists of a light source (Ocean Optics LS1) and a detector attached to it. On two mobile branches, regulating the incident angle of the incoming light, the detector sensors and the collimator are located. The flow cell made of poly(tetrafluoroethene) (PTFE), a synthetic fluoropolymer lays on a goniometer. The device has detection sensibility in the range of ±0.0001 refractive index unit.

SPR measurements were recorded at 27 ^{o}C using a temperature controller system. The solutions used in these experiments were flowed through the apparatus using a peristaltic pump (80 µl/min), and switching between different solutions was achieved via the use of a 6-port valve (Upchurch Scientific). To set a baseline for experimental measurements, TBS solution was first flowed through the apparatus and coated slide. For the conventional method, first 195 µl 20 µg/ml bio-QBP1 in TBS solution, then TBS solution (for washing purpose) and finally 200 µl SA-Q-Dot solution were circulated through the SPR system with the same flowing rate. For the innovative approach, bio-QBP1 and SA-Q-Dot solutions initially were blended and then were flowed through the flow cell. Lastly, for the negative control group measurements, only SA-Q-Dot solution without any peptide was introduced through the flow cell. Both in the innovative approach and negative control group measurements, an identical washing step was followed by running TBS solution though the flow cell for detaching non-specifically bound and unbound peptides or peptide decorated quantum dots from the silica surface. In all three groups, three different green emitting SA-Q-Dot concentrations 1/40, 1/20, and 1/10 diluted from initial concentration (0.0625 µM, 0.125 µM, and 0.250 µM) were presented to observe the effect of different SA-Q-Dot concentration to the experiment. In each case, after a specified interval to allow SA-Q-Dot adsorption onto the silica thin films, TBS solution was flowed through the system to monitor SA-Q-Dot desorption from the target thin film. Collecting data, we also calculated the binding adsorption and desorption rates for each concentration. The equilibrium constants and binding energies were also computed. The surface coverage of SA-Q-Dots in each case, was calculated and given in Figure 6.2, and the SPR slides were scanned using fluorescence microscope. As seen from the Figure 6.2, while in our approach surface coverage is around 15%, the surface coverage of quantum dots is in the range of 1% and 0.5% in conventional and negative control groups, respectively. We observed increase in the surface coverage of quantum dots with increasing quantum dot concentration. We intentionally kept the quantum dot concentrations low to see investigate the relation between surface coverage and quantum dot concentration. To note, the used peptide concentration is sufficient to get high peptide coverage on the surface (see Figure 4.3).

The SPR data were gathered using WinSpectral 1.03 software, which collects the normalized dip spectrum at periodic intervals. This dip is fitted to a 4th degree polynomial function for generating the time-dependent metric sensogram. The adsorption of SA-Q-Dot on silica surface was modelled by using modified Langmuir adsorption models. Calculation of adsorption isotherms from the experimental data is based on fitting using the single Langmuir or modified (i.e., bi-exponential) Langmuir adsorption models. The single isotherm can be described by Equation (1).

$$\frac{d\theta}{dt} = k_a(1-\theta)C - k_d\theta \quad (1)$$

Here, θ is the fraction of the available sites that are covered; k_a, and k_d are the association and dissociation rate constants, respectively; and C is the SA-Q-Dot concentration in molar units. The integration of both sides of Equation (1) gives the change in time-dependent monolayer coverage as given in Equation (2). This equation describes an exponential increase of monolayer coverage as a function of time. $\frac{C}{C+(\mathrm{k_d}/k_a)}$ constant gives the surface coverage when time goes to infinity.

$$\theta(\mathrm{t}) = \frac{C}{C+(\mathrm{k_d}/k_a)}[1-\exp(-(k_aC+k_d)t)] \quad (2)$$

For a given time period and temperature, monolayer formation can be described as a function of time by a single rate constant, called k_{obs}, where $k_{obs} = k_a C + k_d$. The rate constant k_{obs} represent both the adsorption and desorption coefficients as a function of peptide concentration. Substituting this expression in Equation (2) along with the expression for surface coverage $\theta(\infty) = C/[C + (k_d + k_a)]$ leads to Equation (3).

$$\theta(t - t_0) = \theta(\infty)[1 - \exp(-k_{obs}(t - t_0))] \quad (3)$$

Equation (3) is only based on the single Langmuir isotherm model. However, this model cannot describe all protein adsorption processes since in fact many biomolecular reactions at interfaces are more complex. For example, in bi-exponential processes, protein adsorption onto a surface may involve two stages that are governed by different rate constants. Therefore, Equation (3) is required to be modified to reflect the overall observed adsorption process with two different rates. Here, the total fractional surface coverage can be represented in Equation (4).

$$\theta_{obs}(t) = x_1\theta_1(t) + x_2\theta_2(t) = x_1\theta_1(\infty)(1 - \exp(-k_{obs1}t)) + x_2\theta_2(\infty)(1 - \exp(-k_{obs2}t)) \quad (4)$$

where $k_{obs1} = k_{a1}C + k_{d1}$ and $k_{obs2} = k_{a2}C + k_{d2}$ represent the two different stages of the adsorption process at the surface. As a consequence of Equation (4) we observe two different rate constants and two different association and dissociation constants. The adsorption process may happen at faster and slower rates. These two different (fast and slow) adsorption behaviors can be triggered by the heterogeneity of the surface structure of the inorganic surface, the conformational change of the peptide during adsorption. Another possible explanation of two different adsorption rates is attributed to the mass transfer limitation.

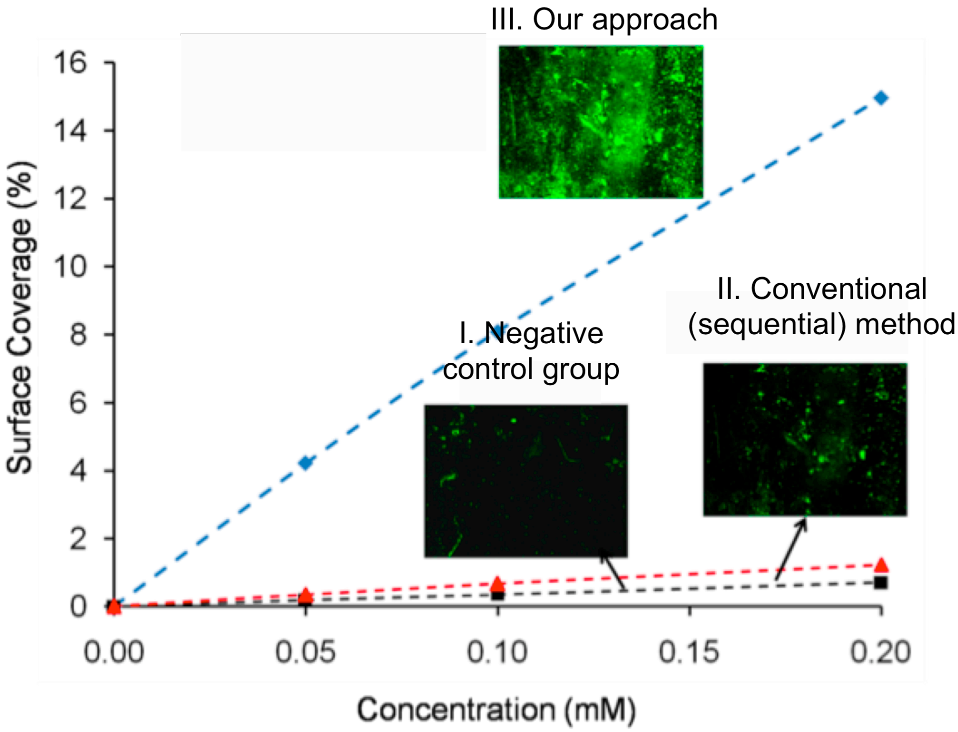

Figure 6.2 – Surface coverage of Q-Dots in convetional, innovative and negative control group experiments.

QCM experiments followed SPR measurements with the same three experimental groups at room temperature to further study real-time dynamics of surface interactions. QCM is commonly used to measure adsorbed mass per unit area by monitoring the change in the resonance frequency of a quartz crystal resonator. Larger shift in the resonance frequency points to a more adsorbed mass on the surface. In our case, we used QCM to investigate kinetics of quantum dots adsorbed on silica surface in three experimental groups. Both conventional, innovative, and negative control group experiments were performed with three different SA-Q-Dot concentrations: 1/120, 1/80, and 1/40 diluted concentrations from the initial one (0.03125 μM, 0.0625 μM and 0.125 μM). For all cases, 10 μg/ml 500 μl, bio-QBP1 was used. Similar to SPR experiments, initially TBS solution was flowed through the QCM system to adjust the baseline. For conventional method, first 500 μl bio-QBP1 and then 500 μl SA-Q-Dot solutions were provided to the silicon oxide coated QCM crystal surface (purchased from

Q-Sense). In our approach, 10 μg/ml 500 μl bio-QBP1 and 500 μl SA-Q-Dot were blended before running from the surface. In negative control group, only 500 μl SA-Q-Dot was introduced to the QCM crystal. In all groups, after SA-Q-Dot flow, TBS buffer was sent to the surface to remove excess amount of SA-Q-Dots and unbound or non-specifically bound ones. QCM experiments indicate better surface coverage with our approach. As seen from Figure 6.3, the biggest shift in resonant frequency is observed in our innovative approach indicating that more quantum dots are adsorbed on the surface.

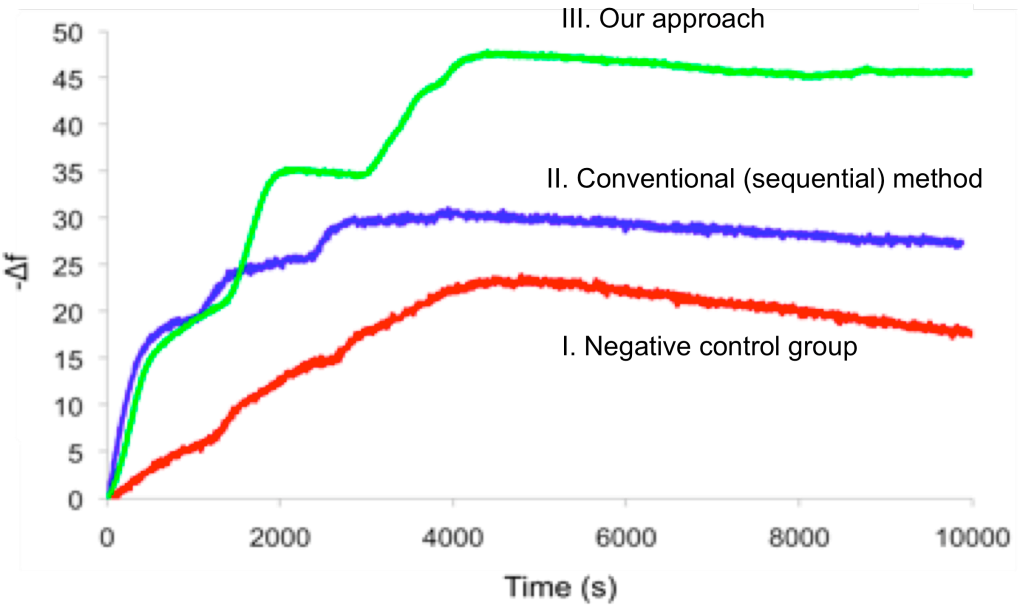

Figure 6.3 – Frequency shift in QCM measurement showing the amount of Q-Dots assembled on the surface in innovative approach, conventional method, and negative control group.

6.2 Multimaterial cross-specificity of smart peptide decorated quantum qot emitters

As a next step, the binding specificity of bio-QBP1 was demonstrated on a real optoelectronic microchip surface which was fabricated for solid-state based lighting applications. For such an optoelectronic chip, there is a need for binding specificity between at least three different types of materials patterned on the same chip; dielectric, metal and semiconductor. As described in Chapter 3, in a previous studies, multi-layered Q-Dot assemblies were achieved using peptide inserted ferritin molecules and this approach was further applied to create nanostructures on Pt patterned surfaces on Ti substrates by utilizing the specific binding of Ti binding peptide [58, 59]. However in these studies, rather than the material specific interaction of peptides, non-specific interactions were utilized. In our experiments for multi-cross-specificity, we first analyzed the binding specificity of bio-QBP1 on Au patterned silica surface and silica patterned Au surfaces in which silica was used as the dielectric and Au as the metal. Working on such two different configurations, we investigated the feasibility of decorating the smaller features of patterned device mesas in complementary geometries in a typical optoelectronic chip.

For the sample preparation, we coated a Si substrate with 50 nm Ti, 500 nm Au, and 50 nm Ti with a thermal evaporator (LH Leybold AG, Inficon IC/4 Deposition Controller). Then, we deposited 300 nm thick silica by using plasma enhanced chemical vapor deposition (PECVD) (Plasma Technology Plasmalab MicroP) at 250 ^{o}C and then patterned different size squares (max. 300 nm along one side) using a mask aligner (Karl Suss MJB 3) and wet etching the silica with hydrofluoric acid (HF). For an alternative way for sample preparation, we also deposited 300 nm thick silica on Si substrate and then 500 nm thick Au for subsequent lift-off to pattern Au film.

Following chip fabrication, both surfaces were incubated with hybrid bio-QBP1-SA-Q-Dots with our approach and then washed as previously described method. Similar to the previous experiments, at room temperature we mixed 100 μg/ml 30 μl bio-QBP1 and 2.5 μM 30 μl SA-Q-Dot and stirred in vortex mixer at 500 rpm before immobilization on chips. Next, the photoluminescence intensities were recorded as a function of wavelength. We measured the photoluminescence with the same photoluminescence set up at room temperature with 2000 μm slit width and 500 ms integration time. Since the spot size of the laser is very small compared to sample surface area (approximately 10 μm diameter), we recorded data from at least three different spots of the same sample for the accuracy of the experiment, then we take average of the each measurement. Moreover, to ensure reproducibility of the results, we repeated the experiment many times with the samples prepared in the same conditions at different times. In Figure 6.4, the photoluminescence intensity of bio-QBP1 assisted assembly of SA-Q-Dots was shown both on Au and silica. Since the bio-QBP1 is only specific to silica but not Au, the photoluminescence intensity peak on the silica part of the chip is 9 times higher than the photoluminescence intensity peak on the Au part. Negative control group experiments were also done by incubating SA-Q-Dots without peptide decoration on the patterned chips. In this case, both on Au and silica part of the chips, the SA-Q-Dots showed significantly lower amount of binding and photoluminescence intensity because of the absence of bio-QBP1.

In addition to Au versus silica binding specificity, another set of binding specificity experiments was carried out with silica (as the dielectric material) versus GaN (as the semiconductor), which is an important component of a light emitting diode (LED) chips. For the GaN/silica chips, we deposited 300 nm thick silica on GaN surface and then patterned it using the same mask aligner setup and following the same etching procedure. For the final step, we again etched silica with HF (hydrofluoric acid). As shown in Figure 6.4, like the silica versus Au experiment we obtained the same result from the binding specificity studies for GaN versus silica experiments. Bio-QBP1-SA-Q-Dots exhibited a very low affinity towards Au and GaN compared to the silica surface. The affinity of the bio-QBP1-SA-Q-Dots was almost at the same ratio compared to the negative control group experiments where we had only SA-Q-Dots, which were not decorated with bio-QBP1.

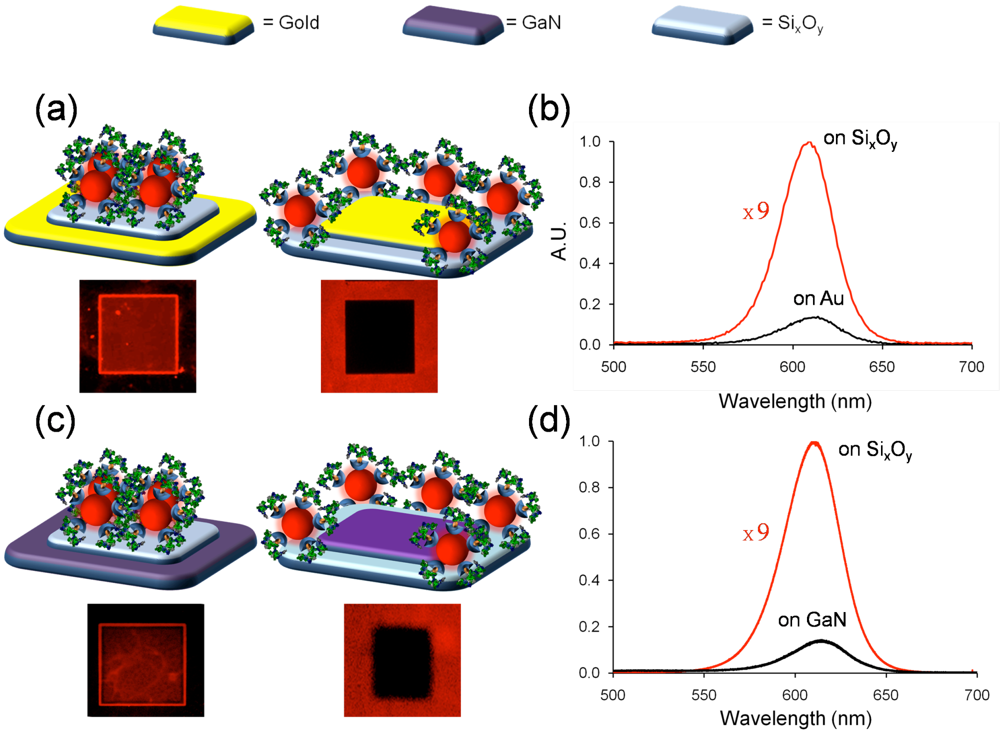

Figure 6.4 Multi-cross-specificity of QBP1-Q-Dots towards silica against both Au and GaN. (a) Specific recognition of the silica surface by QBP1-Q-Dot nanoassembly against Au surfaces in complimentary mesa architectures. QBP1-Q-Dot nanoassemblies were only bound on to silica surface, as QBP1 recognizes silica. The florescence microscopy images of these bound QBP1-Q-Dots are shown along with their corresponding photoluminescence spectra separately from the silica surface (shown in red) and from Au surface (shown in black). The florescence microscopy images clearly indicate specific binding of QBP1-Q-Dot nanoassembly on silica, but not on Au in complementary architecture. The peak photoluminescence intensity of QBP1-Q-Dots assembled on the silica surface is 9 times stronger than that of QBP1-Q-Dots assembled on the Au surface. (b) Cross specificity of the QBP1-Q-Dots towards silica against GaN. The florescence microscopy images clearly show specific binding of QBP1-Q-Dot nanoassembly on silica, but not on GaN. As shown in the associated graph, the peak photoluminescence intensity of QBP1-Q-Dots assembled on silica surface (in red) is 9 times stronger than that of QBP1-Q-Dots assembled on GaN surface (in black).

In previous methods of constructing quantum dot assemblies, the specificity has not been considered. Therefore, in conventional methods, typically many different masking steps were required to pattern quantum dot film in specific regions, which makes the fabrication process comparatively difficult and time-consuming. Another problem of conventional methods is related with the limited mass transfer of quantum dots on the surface, which can lead to systematic problems for creating nanostructures. In our study, we produced and demonstrated hybrid organic-inorganic nano building blocks for photonic applications composed of two main parts, the smart binding part (bio-QBPs) and the optically active part (SA-Q-Dot). Unlike the conventionally created chemical based nanostructures, our hybrid structures exhibit multi-binding specificity. They are specific to silica surface, and their affinity towards silica is not only tested towards silica, but also the binding specificity towards GaN and Au are included.

6.3 Layer-by-layer assembly of quantum dot emitters by peptide mediated biomineralization

6.3.1 Biomineralization

Biomineralization is the phenomenon used by living organisms for 550 millions years to produce minerals inside or outside the cells of organisms, generally to form skeletal structures or strengthen tissues such as sea shells, egg shells in birds and bones in mammals. Silicates in diatoms and algae, calcium phosphates and carbonates in vertebrates, carbonates in diatoms and nonvertebrates, and gold, cupper, and iron in unicellular organisms mainly bacteria exemplify biomineralization in some living organisms [75-77].

Artificial synthesis of minerals and crystals usually necessitates strong conditions such as high temperatures, low pressure, and hazardous chemicals while organisms are capable of depositing these materials in milder condition. On that account, by mimicking the nature, also called biomimetics, it can be more beneficial to produce these minerals via biomineralization. In most cases, minerals do not consist of only one material; in fact they require an organic component, generally milder than pure mineral, which regulates biomineralization process. For instance, during the hard tissue formation, proteins and peptides have been used as key materials for their ability to control the biomineralization.

Inorganic binding peptides are also used in synthesis of various materials such as Au, Ag, Cu_2O, Pt-Co, and Ge nanostructures. In a recent study, controlled biomineralization of hydroxylapatite, which has an important role in the formation of teeth and bones, was reported. Also, titania interlayer in layer-by-layer assembled nanostructures can be synthesized by using the titanium binding peptides. In silica synthesis, mainly a Si containing substance such as tetramethoxysilicate (TMOS), tetraethoxysilicate (TEOS) or another Si containing salt can be used and the biomineralization process is regulated by polyvalent peptides, polymers, or proteins extracted from biological systems. In all these approaches, the molecules used to synthesize silica from a silicon source are utilized in a non-specific random way, except specific interactions of proteins extracted from biological systems. However, to extract a protein from a biological source is tedious since most of the time targeted protein is a cascade protein rather than being a single protein.

6.3.2 Smart peptide controlled silica biomineralization

In previous sections, we described quartz (fused silica) binding peptide mediated self assembly of Q-Dots on silica surface by means of cross-specific binding on multi-material chips and LEDs. In this section we demonstrate another important function of quartz binding peptide, controlled growth of silica from TMOS. Afterwards, QBP1 hybridized Q-Dots are self assembled on biomineralized silica surface through the interaction between silica binding peptide and silica surface. These results are promising for utilizing quartz binding peptide in two different functions, material synthesis, and self assembly towards creating bioenabled nanostructures.

Silica synthesis was performed using TMOS solution as the precursor material at room temperature. TMOS was hydrolyzed in 0.1 M HCl solution to obtain 1 M TMOS as the final concentration and then the biomineralization was initiated by adding 500 μg/ml QBP1, which had been dissolved in TBS solution. To observe the effect of the peptide on silica formation, a control group was also prepared without adding QBP1 in TMOS to compare silica formation with and without peptide. In the negative control group instead of QBP1 TBS solution was used in equal volumes. Final solutions of both groups were dropcasted on diced Si substrates and left in fume hood until the solutions evaporate. Before dropcasting the solutions on the Si substrates, to assure that the substrates do not contain any other oxide layer, possible native silicon oxide layer on Si surfaces were removed by keeping the Si substrates in 1/10 diluted hydrofluoric acid (HF) for 15 minutes. After samples dried, SEM (FEI) and TEM (FEI Tecnai G2 F30, 300kV) images were taken to characterize the synthesized silica surface. In previous studies, it was demonstrated that hydrolysis of TMOS in a mild acidic condition gives rise to the formation of silica. In our study we observed that peptide mediation leads to more controlled structures. As seen from Figure 6.5 (A), in the silica biomineralization without QBP1, silica film has huge particles with cracks on the surface, which shows the lack of restriction in particle size during the silica growth, and hinders the formation of continuous and homogenous silica films. This feature is extremely critical during the formation of layer-by-layer assemblies of nanoparticles by synthesizing silica surface as a separating or an intermediate layer between two nanoparticle layers such as nanocrystals. If the separating layer is not sufficiently uniform, then the nanoparticle assembly on the next layer lacks uniformity as well, which is a serious problem in device fabrication. Also, controllable thickness of the intermediate silica layer plays an important role in layer-by-layer assemblies of nanoparticles. In some devices, the separating layer must be thick enough to provide the desired energy transfer between the two nanoparticle layers, i.e., in localized plasmon enhanced emission of nanocrystal based devices, if one of the layer is made of metal nanoparticles and the other layer is made of nanocrystals, then the silica layer between two layers must be approximately 10 nm to support plasmon enhancement in nanocrystal fluorescence; otherwise, quenching in the nanocrystal luminescence is observed**.**

However, in the case of peptide controlled growth of silica, a more controlled surface structure and topography seem to be formed in Figure 6.5(B). In this approach, the peptides were added into TMOS solution while the silica was formed. QBP1 has a high affinity towards silica surface; the binding energy of QBP1 on silica surface is around -7 kcal mol^{-1}. The interaction of the peptide may occur though the interaction of the side chains; in previous studies, it was concluded that the formation of silica is effected by the charge of the peptides, and in many of these studies polypeptides with positive charge was utilized to form silica platelets and silica surfaces. Additionally, in nature it was also found that some of the biological organisms use polypeptides which are heavily positively charged for the formation of the silica structures. But in our case the QBP1 peptide does not include any charged group in its structure and the total charge of the peptide is zero. So we can conclude that the formation of the silica by using our peptide is triggered by the deposition of the silica on peptide surface, since peptide formes a template for the formation of silica. As seen in Figure 6.5(A), the silica formed under uncontrolled conditions is different then that of peptide controlled synthesis. In peptide controlled synthesis, the growth of silica layer is controlled and restricted in every direction. The formed silica layer surface to be formed in continuum spherical structures, the size of these structures is homogenously distributed.

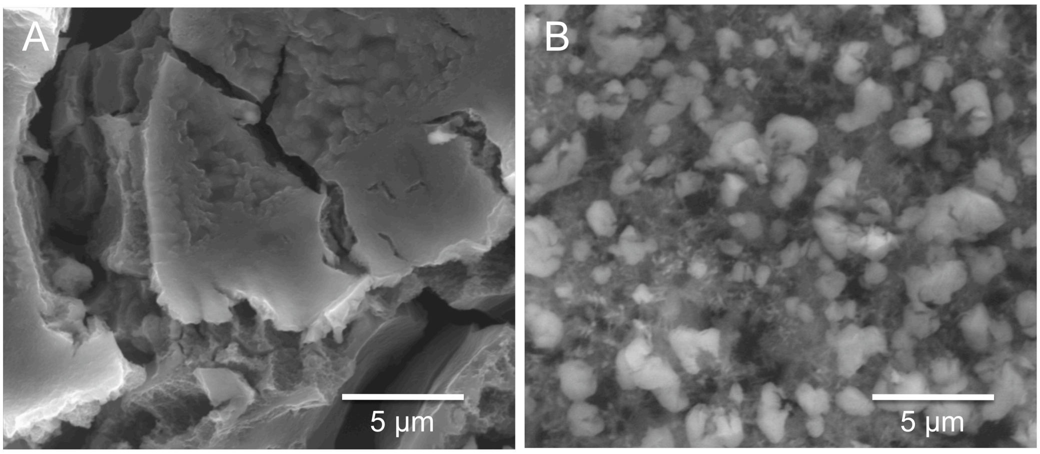

Figure 6.5 - SEM image of silica biomineralization process (A) of control group without QBP1 (B) with QBP1. In control group sample, silica growth is more disordered with giant silica particles on the surface. On the other hand, with peptide assisted silica growth, size of the silica particles have been controlled and limited by the peptide.

In addition to SEM images QBP1 mediated silica growth was characterized with TEM images and diffraction patterns. In this experiments, peptide mediated samples were prepared with 1 mg/ml QBP1 in TBS solution by adding 1 M TMOS pre-hydrolyzed in 1 mM HCl as previously discussed. In control group samples, the same volume of TBS buffer was used. Then, 2 μl of final solutions of both groups was dropped on TEM sample grids and kept in fume hood overnight to dry enough for TEM characterization. In Figure 6.6, TEM images of silica formation without (A) and with (B) peptide are given. TEM images were taken by FEI Tecnai G2 F30 Series with 300kV. In Figure 6.6(A) surface was randomly distributed and any ordered pattern is not observed when we compare with the Figure 6.6(B). In the peptide assisted silica growth as seen in Figure 6.6(B), there is a patterned structure on the silica surface which proves us QBP1 helps silica to grow in a patterned way rather than in an arbitrary and undirected way.

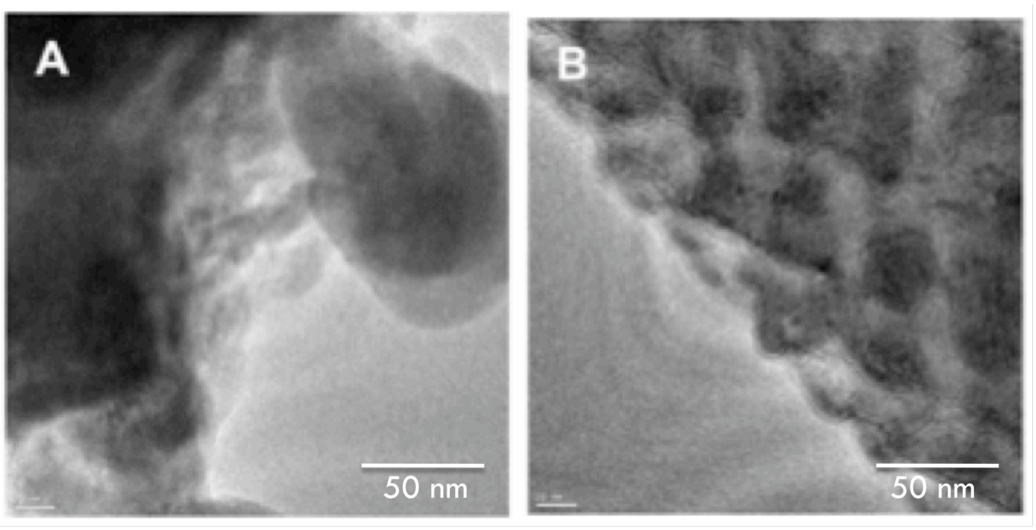

Figure 6.6 – TEM Images of silica growth (A) without QBP1 assistance and (B) with QBP1 assistance.

Also the same samples were investigated for their diffraction patterns. The same TEM machine was used with the same parameters. In diffraction pattern measurements, parallel electron beams are scattered in many different directions while they go into the sample. Scattered electrons are focused on a point in image plane by electromagnetic lens such that electrons arising from the same point of the sample concentrate on the same location in the image plane and then we see the image on the image plane. Also, some electrons are scattered in the same direction even though they arise from different points of the sample. This type of electrons can be focused on the diffraction plane which is located between the lens and the focal plane. We can get diffraction pattern images of the samples as shown in Figure 6.7 by detecting this type of electrons in the diffraction plane which also tells us about the Fourier transform of the image. Diffraction pattern mainly gives information about how electron beams are scattered while they go into the sample and how the angular scattering is distributed according to crystal orientations in a sample. By knowing that one can say that silica growths without peptide and with peptide differ in terms of their crystal structures. In Figure 6.7(A) in the diffraction pattern of silica surface without peptide control, there is diagonal line of dots which means there is a kind of symmetry in one direction which is probably in the z direction, since silica is composed of layered structures. In Figure 6.7(B) there is a completely different kind of symmetry which means different type of crystalline structure. In peptide mediated silica synthesis, silica structure does not have only one directional symmetry due to layered structure but also symmetry in other directions.

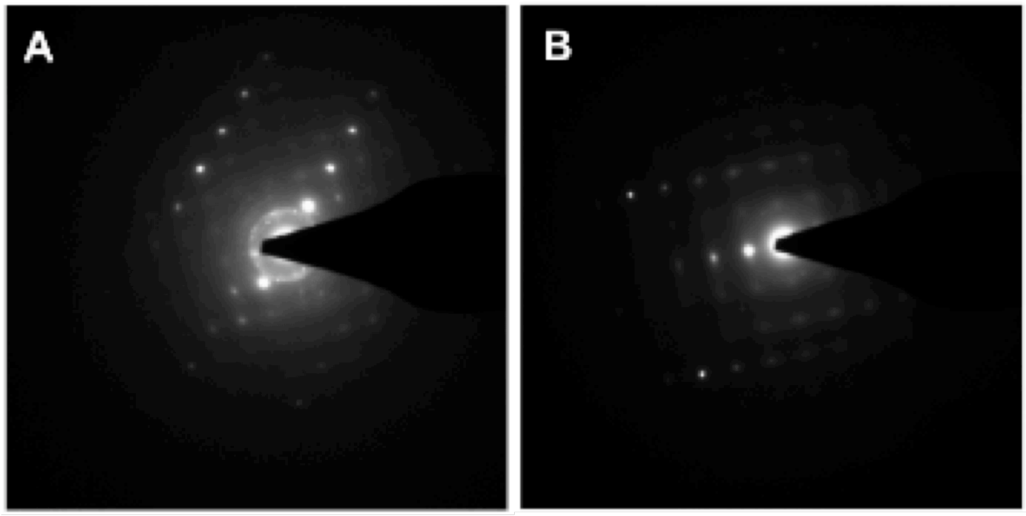

Figure 6.7 – TEM Diffraction patterns of (A) silica synthesis without peptide mediation and (B) with peptide mediation.

At this point, we can say that if the peptide forms the template for the deposition of the silica, than the peptide concentration should be effective in the formation of the silica. To test this, we probed the silica formation as a function of peptide concentration; in this context, the peptide concentration was changed from 50 μg/ml, to 200 μg/ml and finally 800 μg/ml while TMOS was prepared as described before in same conditions at room temperature.

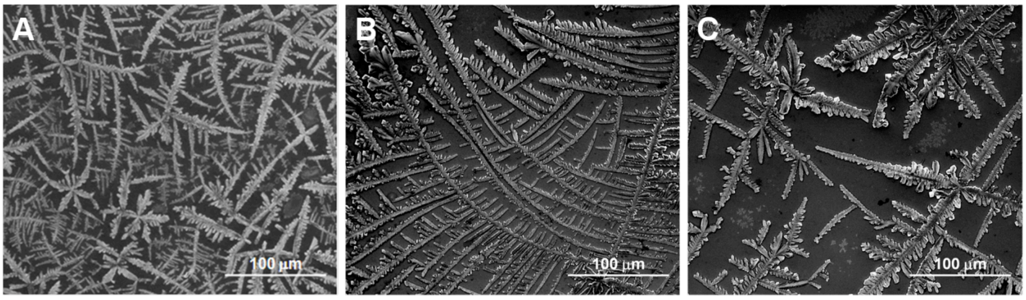

Figure 6.8 – SEM images of silica biomineralization with 50 µm/ml in (A), 200 µm/ml in (B) and 800 µg/ml in (C) different peptide concentrations.

In Figure 6.8, SEM images were sorted from left to right in increasing amount of peptide. In Figure 6.8 the peptide was observed to form branched structures, and as the peptide concentration increases, the density of branched like structures increases as well since the surface coverage increases. This may be the reason that peptide restricts the growth of silica structures. This requires the amount of the peptide to be adjusted carefully to yield a homogenous continuous surface structure.

After the formation of the silica surface, we studied self-assembly of Q-Dots on the synthesized silica surface, since this synthesized silica can be utilized as an intermediate layer in a design of layer-by-layer assembly of nanostructures. To explore this property, we first hybridized Q-Dots with bio-QBP1 as described in previous sections in order to bifunctionally use them, the first one is for the self-assembly of Q-Dots on silica surface by specific binding property and the second one is covering Q-Dot surface to control intermediate silica growth in biomineralization process with the free and unbound terminals of bio-QBP. In this part of the study, we demonstrate the first functionality of hybrid nanostructures on synthesized silica surface subsequently, the study of layer-by-layer assembly of Q-Dots we show the uses of the second functionality at the same time with the first functionality. Silica structures were synthesized in two different ways, one is with the control of QBP1 and the other one is in the absence of QBP1 on Si surface. Native silicon oxide layers were again removed from the surface with HF (1/10 diluted) etching for 15 min to ensure that there was not any silica layer before silica synthesis on the surface. As the next step, green emitting hybrid nanostructures (bio-QBP1-SA-Q-Dots) which have emission peak at 520 nm were drop casted on both of these synthesized silica structures. All samples were washed with TBS solution to remove unbound or non-specifically bound hybrid nanostructures from the surface. Following the assembly of the bio-QBP1-SA-Q-Dot, the confocal images were carried out as shown in Figure 6.9(A), with confocal microscope (Zeiss, EC Plan-Neofluar 20x/0.50 M27 objective). Figure 6.8(A) presents the confocal image of green hybrid nanostructures on silica grown in the absence of QBP1 and Figure 6.9(B) depicts the confocal microscopy image of green hybrid nanostructures on silica grown in the presence of QBP1. In both images, green hybrid nanoassemblies with emission peak at 520 nm were excited at 488 nm. In the confocal imaging, optical emissions with wavelength longer than 515 nm were collected by the detector and in each image an area of 450 μm by 450 μm was scanned. As observed in the images, in silica growth without peptide assistance, the surface has deep and sharp cracks rather than a smooth and continuous surface as in the case of peptide mediated silica growth.

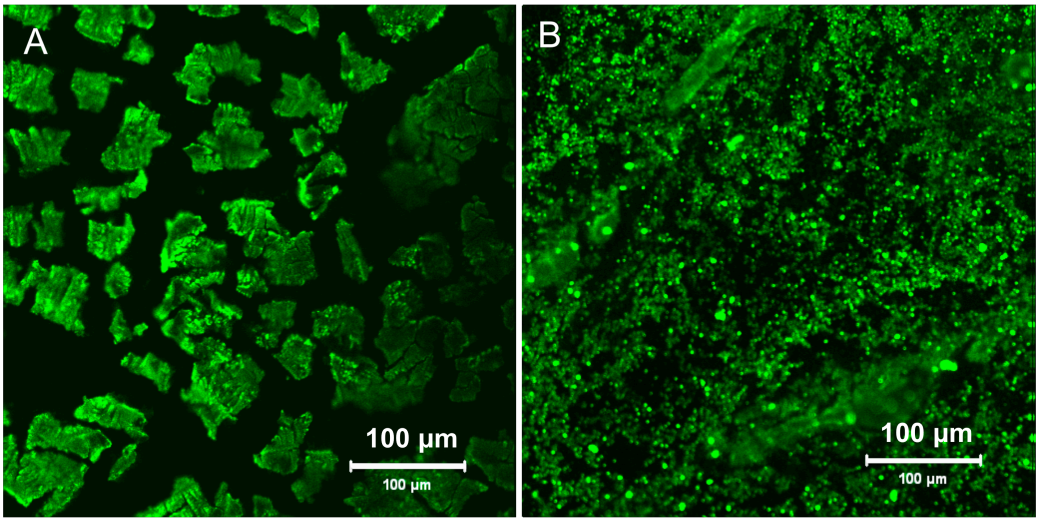

Figure 6.9 – Confocal microscopy images of green (520 nm) emitting bio-QBP1-SA-Q-Dot hybrid nanostructures assembled on silica surface grown (A) without peptide and (B) with peptide.

6.3.3 Peptide controlled biomineralization mediated layer-by-layer assembly of quantum qot emitters

Following the silica biomineralization with the help of QBP1, we tested the silica film in layer-by-layer assemblies of Q-Dots. Layer-by-layer assembly of nanocrystals or metal nanoparticles is very important in design of color conversion LED devices.

Here we first assembled red emitting bio-SA-Q-Dot nano hybrid structures (with emission peak at 620 nm) on quartz surface with the same procedure in previously described assemblies. Then, an intermediate silica layer was synthesized on op of the red emitting bio-QBP1-SA-Q-Dots film in the assistance of free peptide ends of red emitter. After the formation of intermediate silica layer, green emitter bio-QBP1-SA-Q-Dots (with emission peak at 520 nm) were self assembled on silica surface by exploiting strong affinity of QBP1 towards silica. The confocal microscopy image of the overall layer-by-layer structure is shown in Figure 6.10(C). The emissions originating from the red (the first layer) and green (the second layer) emitting nano hybrid assemblies are both collected from distinct channels and corresponding images are shown in Figure 6.10(A) and Figure 6.10(B). The reason why the red emission is stronger than the green emission even though the same amount of emitters were used in each cases, can be explained with higher quantum efficiency of red emitting SA-Q-Dots than green emitting SA-Q-Dots. With this study we demonstrated the existence of silica layer between two hybrid nano assemblies and showed the possibility to form layer-by-layer assemblies of nano structures on top of each other by using peptide mediated grown silica as a separating layer.

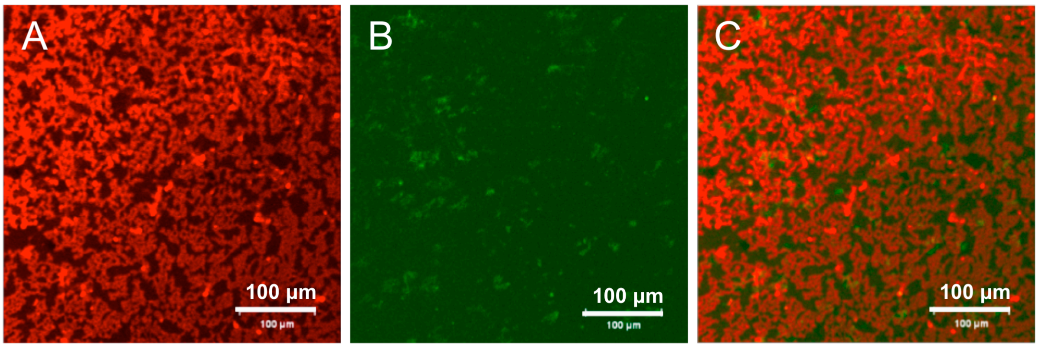

Figure 6.10– Confocal microscopy images of two layers of hybrid nanoassemblies (bio-QBP1-SA-Q-Dots). In (A) is shown the emission arising from the red emitting as the first layer of nanoassemblies. On top of the first layer, silica biomineralization was achieved by free QBP1 terminals of bio-QBP1-SA-Q-Dots. Then green hybrid nanoassemblies (bio-QBP1-SA-Q-Dots) were specifically immobilized on silica surface by self-binding ability of bio-QBP1-SA-Q-Dots on silica surface. The emission originating from green bio-QBP1-SA-Q-Dots is given in (B). Overall emission from the layer-by-layer structure is presented in (C).

Having studied that peptide controlled silica layer can be utilized as the separating layer between two hybrid nanostructures, we studied the effect of the silica layer in the emission of hybrid nanoassemblies. For this purpose, we prepared four different samples. The first sample is green emitting bio-QBP1-SA-Q-Dot immobilized on quartz. The second one is again green emitting bio-QBP1-SA-Q-Dot immobilized on quartz surface but this time it is laid on the peptide mediated synthesized silica surface as described in previous layer-by-layer study.

The third specimen is green emitting bio-QBP1-SA-Q-Dot immobilized on the silica layer, which was synthesized on green emitting bio-QBP1-SA-Q-Dot layer. Finally, the fourth one is red emitting bio-QBP1-SA-Q-Dot assembled on the silica layer, which was grown on green emitting bio-QBP1-SA-Q-Dot layer. For each layer of bio-QBP1-SA-Q-Dot, 2.5 μM 15 μl SA-Q-Dot in water and 100 μg/ml 15 μl bio-QBP1 in TBS were used. 30 μl 0.1 mM TMOS pre-hydrolyzed in HCl was dropcasted on free peptide terminals of bio-QBP1-SA-Q-Dot layer and washed with 200 μl TBS solution to stop the silica formation after 10 min. photoluminescence measurements given in Figure 6.11 were carried out in the same photoluminescence setup described before. Photoluminescence measurements revealed that after formation of a silica layer on top of a green emitting bio-QBP1-SA-Q-Dot layer, its photoluminescence intensity is reduced by significant amount. Another observation from the photoluminescence measurement is that a second layer of green bio-QBP1-SA-Q-Dot compensates for the reduction in the photoluminescence intensity due to the silica absorption even the photoluminescence intensity reaches a higher value from the single layer of bio-QBP1-SA-Q-Dot before the silica growth on it. This experiment was further important to prove formation of intermediate silica layer between two layers of different types of quantum dots. The second layer of red emitting quantum dots on top of green emitting quantum dots is the evidence of the separating silica layer.

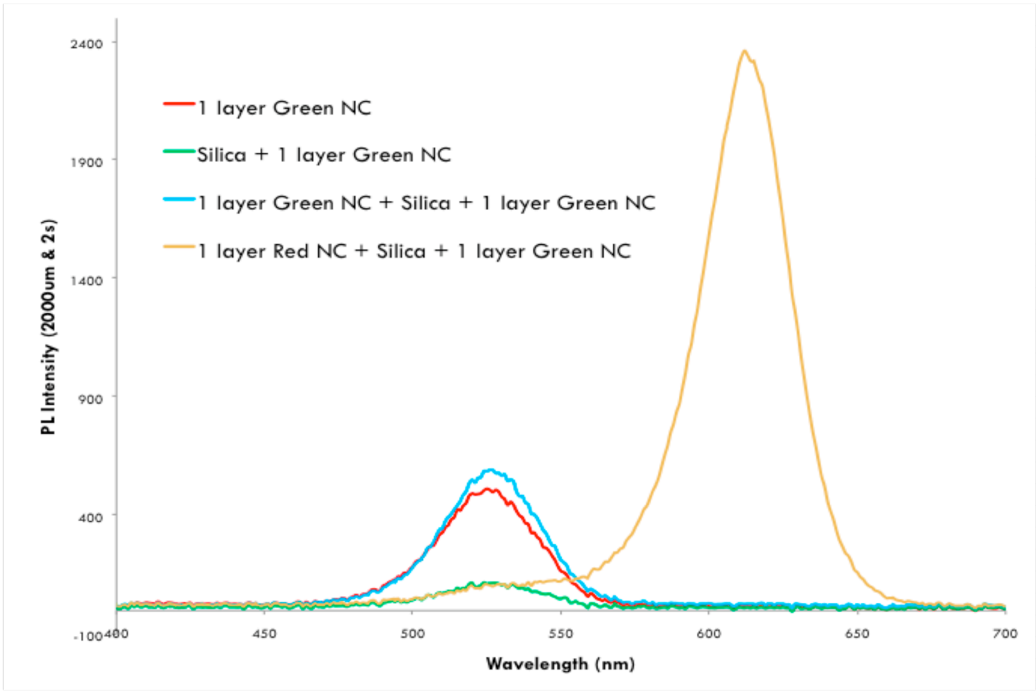

Figure 6.11– Photoluminescence of (A) one layer of green emitting quantum dots, which was coated with peptide mediated silica layer on top. (B) Two layers of quantum dots separated with peptide mediated silica layer. First layer is green emitting quantum dots and second layer is the red emitting quantum dots.

SEM images of each layer are shown in Figure 6.12. Figure 6.12(A) presents the first layer of bio-QBP1-SA-Q-Dot and Figure 6.12(B) depicts the silica growth on bio-QBP1-SA-Q-Dot layer, and finally Figure 6.12(C) gives the second layer of bio-QBP1-SA-Q-Dot on the silica layer.

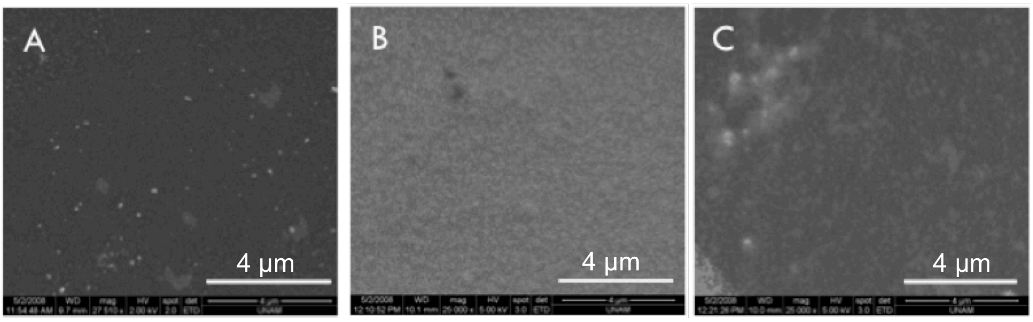

Figure 6.12 – Layer-by-layer structure was characterized by SEM images. The surface of each intermediate level was observed by SEM. (A) Bio-QBP1-SA-Q-Dot layer, (B) intermediate silica layer, and (C) the second layer of bio-QBP1-SA-Q-Dot.

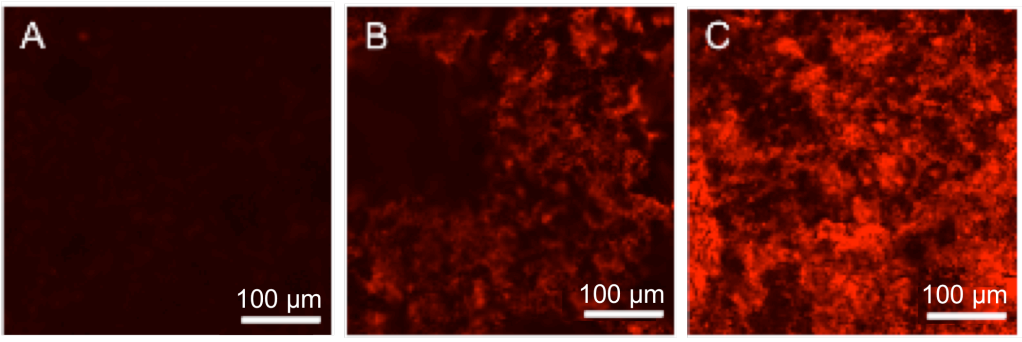

Figure 6.13 – Confocal microscopy images of three layered red emitting hybrid nanoassemblies. (A) The first layer of bio-QBP1-SA-Q-Dot, (B) the second layer of bio-QBP1-SA-Q-Dot, and finally (C) the third layer of bio-QBP1-SA-Q-Dot are shown.

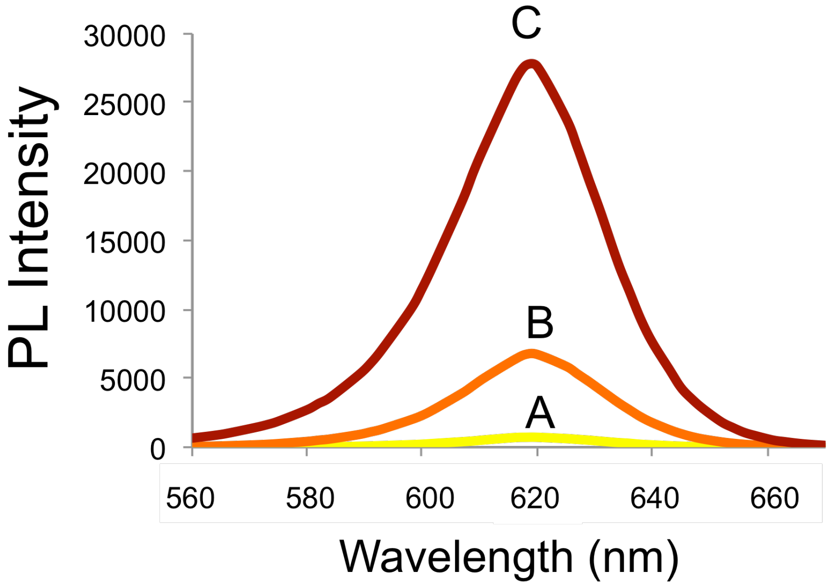

Figure 6.14 – Photoluminescence intensity of three-layered red emitting hybrid nanoassemblies. (A) The first layer of bio-QBP1-SA-Q-Dot, (B) the second layer of bio-QBP1-SA-Q-Dot, and finally in (C) the third layer of bio-QBP1-SA-Q-Dot.

6.4 Peptide assisted assembly of quantum qot emitters on LEDs

Although peptides have been used in the previous studies of our groups and others, this is the first time that multi-specificity of a peptide on a real microchip (on an LED chip) was investigated. We used blue LED for this part of the experiment. The LED epitaxial layers were grown by using a GaN dedicated metal–organic chemical vapor deposition (MOCVD) system (Aixtron RF200/4 RF-S). After deposition of a 14 nm thick GaN nucleation layer and a 200 nm thick GaN buffer layer, we grew a 690 nm thick, Si doped n-type contact layer and InGaN wells, and GaN barriers as the active layers for 462 nm electroluminescence peak. As the final step, we grew p-type layers and GaN layers as the contact cap. During LED fabrication, standard semiconductor processes such as photolithography (Karl Suss MJB-3), thermal evaporator (LH Leybold AG, IC/4 Plus Inficon Deposition Controller), and reactive ion etch (RIE) (LH Leybold AG, LE301) and rapid thermal annealing (AG Associate Mini-Pulse) was used. The composition of n-contacts was 100 nm Ti and 2500 nm Al and then they were annealed at 600 °C for 1 min under N_2 purge. The p-contacts were composed of 15 nm Ni and 100 nm Au and were annealed at 700 °C for 30 s under N_2 purge. Next, 200 nm thick silicon oxide was deposited on the LEDs by using PECVD and then was etched by using RIE after a photolithograph process. Finally, red emitting bio-QBP1 hybridized SA-Q-Dots were incubated on the LEDs and washed with TBS solutions. Confocal microscopy (Carl Zeiss, LSM510 DuoScan) was used to take images of SA-Q-Dots on blue LED, shown in Figure 6.15.

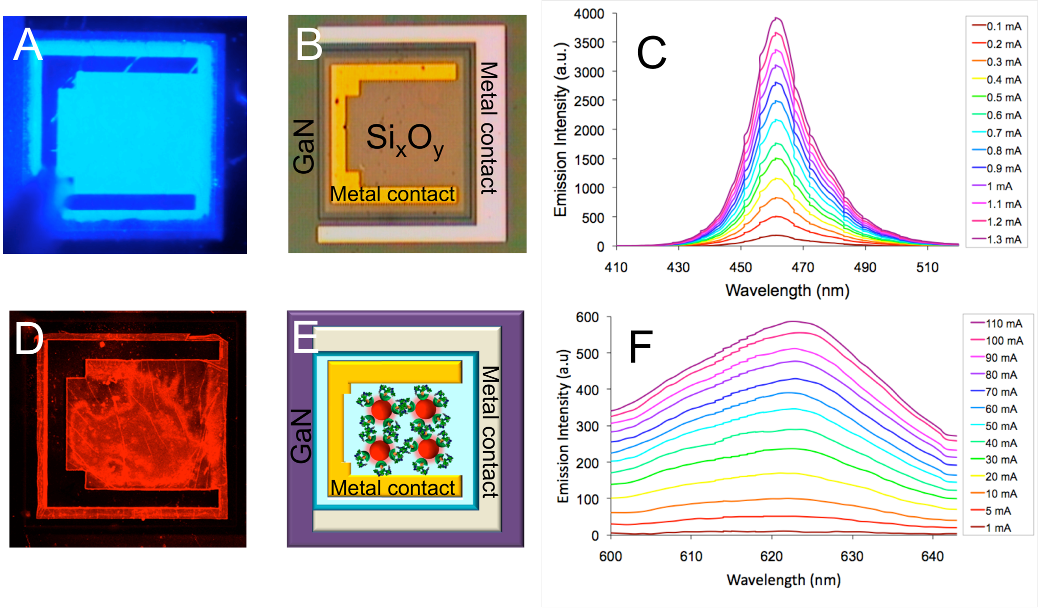

Figure 6.15 – (A) Electroluminescence of the microfabricated LED alone at 462 nm in blue. (B) Plan view of microfabricated LED with the corresponding metal, semiconductor, and dielectric surfaces. (C) Electroluminescence intensity of blue LED with current injection from 0.1 mA to 1.3 mA at 8 V (D) Conformation of the directed self-assembly of the QBP1-Q-Dots on the targeted silica surface of the LED using confocal microscopy. (E) Schematic representation of the LED shown in (B) along with QBP1-Q-Dots (emitting in red at 620 nm) targeted to be assembled specifically on silica on the LED. (F) Photoluminescence of red emitting QBP1-Q-Dots on LED pumped by the blue LED with current injection 1mA to 110 mA at 12 V.

Figure 6.15(F) shows another demonstration of successful directed self-assembly of QBP1-Q-Dots on the targeted silica surface of the blue emitting color-conversion LED. The overall emission of red emitting (620 nm) hybrid nanostructures on blue-LED is provided. Increasing the current injection level increases electroluminescence intensity of blue-LED and also photoluminescence intensity of nanostructures. Furthermore, for the layer-by-layer assembly of Q-Dots, it is important to provide free peptide ends in each layer. These free peptides on Q-Dots, which are not bound on silica surface, will further allow for creating a platform for biomineralization of inner layers for the layer-by-layer assembly.

Chapter 7

Conclusion

In summary, for the first time we demonstrated the material specific targeted self assembly of quantum dot emitters uniformly and reproducibly in terms of optical properties on multi-material patterned color-conversion LEDs by using peptides as smart molecular linkers. Specifically, we use a silica binding peptide, QBP1, which was previously selected using combinatorial genetic selection, with material-specific affinity towards silica, while lacking this affinity towards metal or semiconductor, hence providing a smart molecular building block for the targeted assembly of quantum dots. The peptide quantum dot coupling here is accomplished with molecular recognition characteristics of the biotin streptavidin interaction, where biotin is conjugated to the peptide and streptavidin to the quantum dot. With our innovative approach we experimentally showed 54-fold enhancement in the photoluminescence intensity of the assembled quantum dots compared to conventional method and 270-fold enhancement compared to the control group in which quantum dots are not decorated with peptide. In fact, conventional approach suffers from limited interactions between streptavidin and biotin; therefore, limited diffusion of quantum dots on the surface. Since peptides and quantum dots are sequentially assembled on the substrate, when quantum dots are introduced onto the substrate, streptavidin molecules interact with the stationary biotin molecules stuck on the surface. Innovative approach solves this mass transfer problem between biotin part of the peptides and streptavidin parts of the quantum dots by increasing interactions between them since quantum dots are decorated with peptides in solution through this interaction before immobilization on the surface. Furthermore, we verified the cross-specific binding property of peptide decorated hybrid quantum dots, which was designed to bind silica surface, to silica surface but not to GaN and Au. Experiments revealed that silica binding peptide decorated quantum dots shows 9-fold stronger photoluminescence intensity on silica surface than on GaN or Au surfaces. By our proposed innovative approach, we achieved immobilization of hybrid quantum dots on the desired part of silica coated optical window of our LEDs by distinguishing the targeted surface material from the other materials and binding to this part of the surface showing strong affinity towards it. We demonstrated our results on LEDs with electroluminescence and confocal microscopy measurements. In this thesis we also introduced the use of GEPI as a mediator in silica mineralization process for the intermediate layer between two successive quantum dot film layers. This shows bifunctional use of GEPI in an optoelectronic device and will provide layer-by-layer assembly of not only CdSe/ZnS coreshell quantum dots but also metal and other type of nanoparticles for multi purpose designs. Primarily it will be a tool to assemble different types of quantum dots in different number of layers to tune color parameters of WLEDs such as color rendering index, color temperature, and color coordinates. Secondly it will enable us to design surface plasmon enhancement in the photoluminescence intensity by using metal nanoparticle layers. These results open up new opportunities leading to more specific and controlled assembly and building of novel molecular scale organic-inorganic hybrid devices.

BIBLIOGRAPHY

[1] H. S. Chen, D. M. Yeh, C. Lu, C. Huang, W. Shiao, J. Huang, C. C. Yang, I. Liu, and W. Su, “White Light Generation With CdSe-ZnS Nanocrystals Coated on an InGaN-GaN Quantum-Well Blue/Green Two-Wavelength Light-Emitting Diode,” *IEEE Photonics Technology Letter,* 2006, vol. 18, pp. 1430-1432.

[2] H. S. Chen, C. Hsu, and H. Hong, “InGaN–CdSe–ZnSe Quantum Dots White LEDs,” *IEEE Photonics Technology Letter,* 2006, vol. 18, pp. 193-195.

[3] M. Achermann, M. A. Petruska, D. D. Koleske, M. H. Crawford, and V. I. Klimov, “Nanocrystal-Based Light-Emitting Diodes Utilizing High-Efficiency Nonradiative Energy Transfer for Color Conversion,” *Nano Letters,* 2006, vol. 6, pp. 1396-1400.

[4] P. Bhattacharya, S. Ghosh, and A. D. Stiff-Roberts, “Quantum Dot Opto-Electornic Devices,” *Annual Review Materials Research,* 2004, vol. 34, pp. 1-40.

[5] S. Lee, C. Mao, C. E. Flynn, and A. M. Belcher, “Ordering Quantum Dots Using Genetically Engineered Viruses,” *Science,* 2002, vol. 296, pp. 892-895.

[6] J. P. Mathias, E. E. Simanek, and G. M. Whitesides, “Self- Assembly through Hydrogen Bonding: Peripheral Crowding-A New Strategy for the Preparation of Stable Supramolecular Aggregates Based on Parallel, Connected CA3eM3 Rosettes,” *Journal of the American Chemical Society*, 1994, vol. 116, pp. 4326-4340.

[7] X. Duan, J. Wang, and C. M. Lieber, “Synthesis and Optical Properties of Gallium Arsenide Nanowires,” *Appl. Phys. Lett.*, 2000, vol. 76, pp. 1116-1118.

[8] D. J. Norris, and M. G. Bawendi, “Measurement and Assignment of the Size-Dependent Optical Spectrum in CdSe Quantum Dots,” *Phys. Rev. B 53*, 1996, vol. 53, pp. 16338 - 16346.

[9] . C. E. Fowler, W. Shenton, G. Stubbs, and S. Mann, “Tobacco Mosaic Virus Liquid Crystals as Templates for the Interior Design of Silica Mesophases and Nanoparticles,” *Advanced Materials*, 2000, vol. 13, pp. 1266-1269.

[10] . C. E. Fowler, W. Shenton, G. Stubbs, and S. Mann, “Polyelectrolyte-Quantum Dot Multilayer Films Fabricated by Combined Layer-by-Layer Assembly and Langmuir-Schaefer Deposition,” *Langmuir*, 2004, vol. 20, pp. 2057-2059.

[11] S. Nizamoglu and H. V. Demir, "Nanocrystal based hybrid white light generation with tunable color parameters," *J. Opt. A: Pure Appl. Opt., Special Issue on Nanophotonics*, 200, 9(9), pp. S419-S424.

[12] A. J. Nozik, "Quantum Dot Solar Cells," *Physica E*, 2002, vol. 14, pp. 115-120.

[13] M. Dahan, S. Levi, C. Luccardini, P. Rostaing, B. Riveau, and A. Triller, “Diffusion Dynamics of Glycine Receptors Revealed by Single-Quantum Dot Tracking,” *Science*, 2003, vol. 302, pp. 442-445.

[14] H. Eisler, V. C. Sundar, M. G. Bawendi, M. Walsh, H. I. Smith and V. Klimov, “Color-selective Semiconductor Nanocrystal Laser,” *Appl. Phys.*

Lett., 2002, vol. 80, pp. 4614-4616.

[15] X. Michalet, F. F. Pinaud, L. A. Bentolila, J. M. Tsay, S. Doose, J. J. Li, G. Sundaresan, A. M. Wu, S. S. Gambhir, and S. Weiss, "Quantum Dots for Live Cells, in Vivo Imaging, and Diagnostics," *Science*, 2005, vol. 307, pp. 538-544.

[16] D. L. Kleina, R. Rothb, A. K. L. Limb, A. P. Alivisatosb, and P. L. McEuena, "A Single-electron Transistor Made From a Cadmium Selenide Nanocrystal," *Nature*, 1997, vol. 389, pp. 1-3.

[17] C. B. Murray, D. J. Norris, and M. G. Bawendi, "Synthesis and Characterization of Nearly Monodisperse CdE (E = Sulfur, Selenium, Tellurium) Semiconductor Nanocrystallites," *J. Am. Chem. Soc.,* 1993, vol. 115, pp. 8706-8715.

[18] H. Mattoussi, A. W. Cumming, C. B. Murray, M. G. Bawendi and R. J. Ober, "Characterization of CdSe Nanocrystallite Dispersions by Small Angle X-ray Scattering," *J. Chem. Phys.*, 1996, vol. 105, no. 22, pp. 9890-9896.

[19] H. Mattoussi, A. W. Cumming, C. B. Murray, M. G. Bawendi and R. J. Ober, "Properties of CdSe Nanocrystal Dispersions in the Dilute Regime: Structure and Interparticle Interactions," *Phys. Rev. B*, 1998, vol. 58, no. 12, pp. 7850-7863.

[20] V. L. Colvin, M. C. Schlamp, A. P. Alivisatos, "Light-emitting diodes Made From Cadmium Selenide Nanocrystals and a Semiconducting Polymer," *Nature,* 1994, vol. 370, pp. 354-356.

[21] B. O. Dabbousi, M. G. Bawendi, O. Onitsuka, and M. F. Rubner, “Electroluminescence from CdSe Quantum-dot/polymer Composites,” *Appl.*
Phys. Lett., 1995, vol. 66, pp. 1316-1318.

[22] M. C. Schlamp, X. G. Peng, A. P. Alivisatos, “Improved Efficiencies in Light Emitting Diodes Made with CdSe(CdS) Core/Shell Type Nanocrystals and a Semiconductor Polymer,” *J. Appl. Phys.* 1997, vol. 82, 5837-5842.

[23] H. Mattoussi, L. H. Radzilowski, B. O. Dabbousi, El. L. Thomas, M. G. Bawendi, and M. F. Rubner, “Electroluminescence From Heterostructures of Poly(phenylene vinylene) and Inorganic CdSe Nanocrystals,” *J. Appl. Phys.* 1998, vol. 83, pp. 7965-7974.

[24] H. Mattoussi, L. H. Radzilowski, B. O. Dabbousi, D. E. Fogg, R. R. Schrock, El. L. Thomas, M. F. Rubner, and M. G. Bawendi, “Composite Thin Films of CdSe Nanocrystals and a Surface Passivating/Electron Transporting Block Copolymer: Correlations Between Film Microstructure by Transmission Electron Microscopy and Electroluminescence,” *J. Appl. Phys.,* 1999, vol. 86, pp. 4390-4399.

[25] A. D. Yoffe, “Semiconductor Quantum Dots and Related Systems: Electronic, Optical, Luminescence and Related Properties of Low Dimensional Systems,” *Advances in Physics*, 2001, vol. 50, pp. 1-208.

[26] M. A. Hines, P. J. Guyot-Sionnest, “Bright UV-Blue Luminescent Colloidal ZnSe Nanocrystals,” *Journal of Physical Chemistry B,* 1998, vol. 102, pp. 3655- 3657.

[27] K. Wundke, S. Potting, J. Auxier, A. Schulzgen, N. Peyghambarian, N. F.

Borrelli, “PbS Quantum-dot-doped Glasses for Ultrashort-Pulse Generation,” *Appl. Phys. Lett.,* 2000, vol. 76, pp. 10-12.

[28] M. A. Hines, and P. Guyot-Sionnest, “Synthesis and Characterization of Strongly Luminescing ZnS-Capped CdSe Nanocrystals,” *J. Phys. Chem.,* 1996, vol. 100, pp. 468- 471.

[29] B. O. Dabbousi, J. Rodrigez-Viejo, F. V. Mikulec, J. R. Heine, H. Mattoussi, R. Ober, K. J. Jensen, and M. G. Bawendi, “(CdSe)ZnS Core-Shell Quantum Dots: Synthesis and Characterization of a Size Series of Highly Luminescent Nanocrystallites” *J. Phys. Chem.,* 1997, vol. 101, pp. 9463-9475.

[30] X Peng, M. C. Schlamp, A. V. Kadavanich, and A. P. Alivisatos, “Epitaxial Growth of Highly Luminescent CdSe/CdS Core/Shell Nanocrystals with Photostability and Electronic Accessibility.” *J. Am. Chem. Soc.,* 1997, vol. 119, pp. 7019-7029.

[31] X. Michalet, F. F. Pinaud, L. A. Bentolila, J. M. Tsay, S. Doose, J. J. Li, G. Sundaresan, A. M. Wu, S. S. Gambhir, and S. Weiss, “Quantum Dots for Live Cells, in Vivo Imaging, and Diagnostics,” *Science*, 2005, vol. 307, pp. 538-544.

[32] C. de Mello Donegá, P. Liljeroth, D. Vanmaekelbergh, “Physicochemical Evaluation of the Hot-Injection Method, a Synthesis Route for Monodisperse Nanocrystals,” *Small*, 2005, vol. 12, pp. 1152-1162.

[33] C. B. Murray, and C. R. Kagan, “Synthesis and Characterization of Monodisperse Nanocrystals and Close-Packed Nanocrystal Assemblies,” *Annual Review of Material Science*, 2000, vol. 30, pp. 545-610.

[34] S. Nizamoglu, E. Mutlugun, O Akyuz, N. Kosku Perkgoz, H. V. Demir, L. Liebscher, S. Sapra, N. Gaponik, and A. Eychmüller, “White Emitting CdS Quantum Dot Nanoluminophores Hybridized on Near-Ultraviolet LEDs for High-Quality White Light Generation and Tuning,” *New Journal of Physics*, 2008, vol. 10, pp. 1-9.

[35] T. Jamiesona, R. Bakhshia, D. Petrovaa, R. Pococka, M. Imanib, and A. M. Seifaliana, “Biological Applications of Quantum Dots,” *Biomaterials*, 2007, vol. 28, pp. 4717-4732.

[36] I. L. Medintz, H. T. Uyeda, E. R. Goldman, and H. Mattoussi, “Quantum Dot Bioconjugates for Imaging, Labelling and Sensing,” *Nature Materials*, 2005, vol. pp. 435-446.

[37] M. Dahan, T. Laurence, F. Pinaud, D. S. Chemla, A. P. Alivisatos, M. Sauer, and S. Weiss “Time-Gated Biological Imaging by Use of Colloidal Quantum Dots,” *Optics Letter,* 2001, vol. 26, pp. 825–827.

[38] R. D. Schaller and V. I. Klimov, “High Efficiency Carrier Multiplication in PbSe Nanocrystals: Implications for Solar Energy Conversion,” *Physical Review Letters*, 2004, vol. 24, pp. 1-4.

[39] I. Gur, N. A. Fromer, M. L. Geier, and A. P. Alivisatos, “Air-Stable All-Inorganic Nanocrystal Solar Cells Processed from Solution,” *Science*, 2005, vol. 310, pp. 462-465.

[40] S. Kinge, M. Crego-Calama, and D. N. Reinhoudt, “Self-Assembling Nanoparticles at Surfaces and Interfaces,” *ChemPhysChem*, vol. 9, pp. 20-42.

[41] C. P. Collier, T. Vossmeyer, and J. R. Heath, “Nanocrystal Superlattices,” *Annual Review of Physical Chemistry*, 1998, vol. 49. pp. 371-404.

[42] O. Ikkala, and G. ten Brinke, “Functional Materials Based on Self-Assembly of Polymeric Supramolecules,” *Science,* 2002, vol. 295, pp. 2407 – 2409.

[43] N. D. Denkov, O, D. Velev, P. A. Kralchevsky, I. B. Ivanov, H. Yoshimura and K. Nagayama, “Two-Dimensional Crystallization,” *Nature,* 1993, vol. 361, pp. 26.

[44] E. Rabani, D. R. Reichman, P. L. Geissler and Louis E. Brus, “Drying-Mediated Self-Assembly of Nanoparticles,” *Nature*, 2003, vol.426, pp. 271-274.

[45] C. J. Brinker, Y. Lu, A. Sellinger, and H. Fan, “Evaporation-Induced Self-Assembly: Nanostructures Made Easy,” *Advanced Materials*, 1999, vol. 11, pp. 579-585.

[46] P. C. Ohara, D. V. Leff, J. R. Heath and W. M. Gelbart, “Crystallization of Opals from Polydisperse Nanoparticles,” *Physical Review Letters,* 1995, vol. 75, pp. 3466-3470.

[47] T. P. Bigioni, X. M. Lin, T. T. Nguyen, E. I. Corwin, T. A. Witten, and H. M. Jaeger, “Kinetically Driven Self Assembly of Highly Ordered Nanoparticle Monolayers,” *Nature Materials*, 2006, vol. 5, pp. 265–270.

[48] P. Jonkheijm, P. van der Schoot, A. P. H. J. Schenning, and E. W. Meijer, “Probing the Solvent-Assisted Nucleation Pathway in Chemical Self-Assembly,” *Science*, 2006, vol. 313, pp. 80-83.

[49] J. H. Fendler, “Chemical Self-assembly for Electronic Applications,” *Chem. Mater.*, 2001, vol. 13, pp. 3196-3210.

[50] H. Ma, M. T. Zin, M. H. Zareie, M. Kang, S. Kang, K. Kim, B. W. Reed, C. T. Behar, M. Sarikaya and A. K. Y. Jen, “Assembly of Nanomaterials Through Highly Ordered Self-Assembled Monolayers and Peptide-Organic Hybrid Conjugates as Templates,” *Journal of Nanoscience and Nanotechnology*, 2007, vol. 7, pp. 2549-2566.

[51] R. Zirbs, F. Kienberger, P. Hinterdorfer, and W. H. Binder, “Directed Assembly of Au Nanoparticles onto Planar Surfaces via Multiple Hydrogen Bonds,” *Langmuir,* 2005, vol. 21, pp. 8414-8421.

[52] G. M. Lowman, S. L. Nelson, S. M. Graves, G. F. Strouse, and S. K. Buratto, “Polyelectrolyte-Quantum Dot Multilayer Films Fabricated by Combined Layer-by-Layer Assembly and Langmuir-Schaefer Deposition,” *Langmuir* 2004, vol. 20, pp. 2057-2059.

[53] K. M. Lenahan, Y. Wang, Y. Liu, R. O. Claus, J. R. Heflin, D. Marciu, and C. Figura, “Novel Polymer Dyes for Nonlinear Optical Applications Using Ionic Self-Assembled Monolayer Technology,” *Advanced Materials*, 1999, vol. 10, pp. 853-855.

[54] K. D. Hermanson, S. O. Lumsdon, J. P. Williams, E. W. Kaler, and O. D. Velev, “Dielectrophoretic Assembly of Electrically Functional Microwires from Nanoparticle Suspensions,” *Science,* 2001, vol. 294, pp. 1082–1086.

[55] M. A. Correa-Duarte and L. M. Liz-Marzán, "Carbon Nanotubes as Templates for One-Dimensional Nanoparticle Assemblies," *J Mater. Chem.*, 2006, vol. 16, pp. 22-25.

[56] J. Sharma, Y. Ke, C. Lin, R. Chhabra, Q. Wang, J. Nangreave, Y. Liu, and H. Yan, "DNA-Tile-Directed Self-Assembly of Quantum Dots into Two-Dimensional Nanopatterns," *Angew. Chem. Int. Ed.*, 2008, vol. 47, 5157 – 5159.

[57] G. P. Mitchell, C. A. Mirkin, and R. L. Letsinger, "Programmed Assembly of DNA Functionalized Quantum Dots," *J. Am. Chem. Soc.,* 1999, vol. 121, pp. 8122-8123 .

[58] K. Sano, H. Sasaki, and K. Shiba "Utilization of the Pleiotropy of a Peptidic Aptamer To Fabricate Heterogeneous Nanodot-Containing Multilayer Nanostructures," *J. Am. Chem. Soc.,* 2006, vol. 128, pp. 1717-1722.

[59] K. Sano, S. Yoshii, I. Yamashita, and K. Shiba, "In Aqua Structuralization of a Three-Dimensional Configuration Using Biomolecules," *Nano Letters*, 2007 vol. 7, pp. 3200-3202.

[60] M Sarikaya, C Tamerler, D. T. Schwartz, and F. Baneyx, "Materials Assembly and Formation Using Engineered Polypeptides," *Annual Review Materials Research,* 2004, vol.34, pp. 373-408.

[61] C. Tamerler, M. Duman, E. E. Oren, M. Gungormus, X. Xiong, T. Kacar, B. A. Parviz, and M. Sarikaya "Materials Specificity and Directed Assembly of a Gold-Binding Peptide," *Small*, 2006, vol. 2, pp. 1372-1378.

[62] M. Sarikaya, “Biomimetics: Materials fabrication through biology,” *Proceedings of the National Academy of Sciences*, 1999, vol. 96, pp. 14183-14185.

[63] C. Mao, C. E. Flynn, A. Hayhurst, R. Sweeney, J. Qi, G. Georgiou, B. Iverson, and A. M. Belcher, “Viral Assembly of Oriented Quantum Dot Nanowires,” *PNAS,* 2003, vol. 100, pp. 6946-6951.

[64] M Sarikaya, C Tamerler, AKY Jen, K Schulten, and F. Baneyx, “Molecular Biomimetics: Nanotechnology Through Biology,” *Nature Materials,* 2003, vol. 2, pp. 577-585.

[65] C. Tamerler, and M. Sarikaya “Molecular biomimetics: Utilizing nature’s molecular ways in practical engineering,” *Acta Biomaterialia 3*, 2007, pp. 289-299.

[66] Y. Chen, and D. E. Rodak, “Is the Lotus Leaf Superhydrophobic?” *Appl. Phys. Lett.,* 2005, vol. 86, pp. 1-4.

[67] C. Tamerler, T. Kacar, D. Sahin, H. Fong, M. Sarikaya, “Genetically Engineered Polypeptides for Inorganics: A utility in Biological Materials Science and Engineering”, *Materials Science and Engineering*, 2007, pp. 558-564.

[68] E. E. Oren, C. Tamerler, D. Sahin, M. Hnilova, U. O. S. Seker, M. Sarikaya, and R. Samudrala, “A novel knowledge-based approach to design inorganic-binding peptides,” *Bioinformatics*, 2007, vol. 23, no. 21, pp. 2816–2822.

[69] U. O. S. Seker, B. Wilson, S. Dincer, W. Kim, E. E. Oren, J. S. Evans, C. Tamerler, and M. Sarikaya, “Adsorption Behavior of Linear and Cyclic

Genetically Engineered Platinum Binding Peptides," *Langmuir*, 2007, vol. 23, pp. 7895-7900.

[70] E. F. Schubert, *Light-emitting diodes: research, manufacturing and applications VI.* Cambridge University Press, 2002.

[71] S. Nizamoglu, G. Zengin, and H. V. Demir, "Color-converting Combinations of Nanocrystal Emitters for Warm-white Light Generation with High Color Rendering Index", *Applied Physics Letters*, 2008, vol. 92, 031102.

[72] S.Nizamoglu, E. Mutlugun, T. Ozel, H. V. Demir, S. Sapra, N. Gaponik, and A. Eychmüller, "Dual-color Emitting Quantum-dot-quantum-well CdSe-ZnS Heteronanocrystals Hybridized on InGaN / GaN Light Emitting Diodes for High-quality White Light Generation", *Applied Physics Letters*, 2008, vol. 92, no. 113110.

[73] S. Nizamoglu and H. V. Demir, "Hybrid white light sources based on layer-by-layer assembly of nanocrystals on near-UV emitting diodes," *Nanotechnology*, 2007, vol. 18, 405702.

[74] S. Nizamoglu, T. Ozel, E. Sari, and H. V. Demir, "White light generation using CdSe/ZnS core-shell nanocrystals hybridized with InGaN/GaN light emitting diodes," *Nanotechnology*, 2007, vol. 18, 065709.

[75] A. L. Boskey, "Biomineralization: An Overview," *Connective Tissue Research,* 2003, vol. 44, pp. 5-9.

[76] L. Addadi, and S. Weiner, "Control and Design Principles in Biological Mineralization," *Angewandte Chemie International Edition in English,* 1992, vol. 31, pp. 153–169.

[77] S. Weiner, and L. Addadi, “Design Strategies in Mineralized Biological Materials,” *J. Mater. Chem.,* 1997, vol. 7, pp. 689-702.